

REPORT DOCUMENTATION PAGE

Form Approved
OMB No. 0704-0188

The public reporting burden for this collection of information is estimated to average 1 hour per response, including the time for reviewing instructions, searching existing data sources, gathering and maintaining the data needed, and completing and reviewing the collection of information. Send comments regarding this burden estimate or any other aspect of this collection of information, including suggestions for reducing the burden, to the Department of Defense, Executive Services and Communications Directorate (O704-0188). Respondents should be aware that notwithstanding any other provision of law, no person shall be subject to any penalty for failing to comply with a collection of information if it does not display a currently valid OMB control number.

PLEASE DO NOT RETURN YOUR FORM TO THE ABOVE ORGANIZATION.

1. REPORT DATE (DD-MM-YYYY)	2. REPORT TYPE	3. DATES COVERED (From - To) 01 MAR 2004 - 28 FEB 2007		
4. TITLE AND SUBTITLE MICRO-STRESS BOUND ESTIMATE ENABLED OPTIMIZATION OF STRUCTURAL COMPOSITE REPAIR FOR THE NEXT GENERATION AIRCRAFT		5a. CONTRACT NUMBER 5b. GRANT NUMBER FA9550-04-1-0142 5c. PROGRAM ELEMENT NUMBER 2304/BX		
6. AUTHOR(S) PROFESSOR IARVE		5d. PROJECT NUMBER 61102F 5e. TASK NUMBER 5f. WORK UNIT NUMBER		
7. PERFORMING ORGANIZATION NAME(S) AND ADDRESS(ES) UNIVERSITY OF DAYTON 300 COLLEGE PARK AVE DAYTON OH 45469			8. PERFORMING ORGANIZATION REPORT NUMBER	
9. SPONSORING/MONITORING AGENCY NAME(S) AND ADDRESS(ES) AF OFFICE OF SCIENTIFIC RESEARCH 875 NORTH RANDOLPH STREET ROOM 3112 ARLINGTON VA 22203 DR ARJE NACHMAN/NE			10. SPONSOR/MONITOR'S ACRONYM(S) 11. SPONSOR/MONITOR'S REPORT MIMER(S)	
12. DISTRIBUTION/AVAILABILITY STATEMENT DISTRIBUTION STATEMENT A: UNLIMITED		AFRL-SR-AR-TR-07-0266		
13. SUPPLEMENTARY NOTES				
14. ABSTRACT The completed effort integrated the rigorous microlevel (fiber, matrix, sizing) stress bound recently obtained by Lipton [1,2] under AFOSR sponsorship with the AFRL-developed ply level multibasis spline approximation stress analysis tools [3-5]. A robust multiscale analysis framework was developed and applied within and beyond the scope of the present grant. The developments included extension of the stress bound estimates in heterogeneous materials with periodic microstructure to include residual stress effects and, notably, regions of nonperiodic microstructure. Such regions included ply interfaces in fiber reinforced composite materials, which are present in all laminated composite structures. The improved accuracy of the multiscale analysis was verified by comparison with three-dimensional analysis of model cross ply composite laminate, where fibers were modeled explicitly.				
15. SUBJECT TERMS				
16. SECURITY CLASSIFICATION OF: a. REPORT b. ABSTRACT c. THIS PAGE		17. LIMITATION OF ABSTRACT	18. NUMBER OF PAGES	19a. NAME OF RESPONSIBLE PERSON 19b. TELEPHONE NUMBER (Include area code)

University of Dayton Research Institute

Endel V. Iarve

**Micro-stress bound estimate enabled optimization of structural composite repair for
the next generation aircraft**

Final Report

FY04-06

Grant: FA0550-04-1-0142

ABSTRACT The completed effort integrated the rigorous microlevel (fiber, matrix, sizing) stress bound recently obtained by Lipton [1,2] under AFOSR sponsorship with the AFRL-developed ply level multibasis spline approximation stress analysis tools [3-5]. A robust multiscale analysis framework was developed and applied within and beyond the scope of the present grant. The developments included extension of the stress bound estimates in heterogeneous materials with periodic microstructure to include residual stress effects and, notably, regions of nonperiodic microstructure. Such regions included ply interfaces in fiber reinforced composite materials, which are present in all laminated composite structures. The improved accuracy of the multiscale analysis was verified by comparison with three-dimensional analysis of model cross ply composite laminate, where fibers were modeled explicitly. Our analysis capability for the first time addressed the composition of the repair patch of a composite scarf repair in addition to more conventional geometric parameters, such as scarf angle and repair depth. We found that altering the conventional ply by ply replacement schema of the repair patch does not lead to premature failure, but may delay the failure of the adhesive and increase the strength of the repaired composite. This work is well coordinated with the Materials Integrity Branch of the Air Force Research Laboratory's Materials and Manufacturing Directorate, which is presently executing an experimental program to verify our findings. We have transitioned the periodic RVE based micromechanical failure criterion evaluation algorithm to Sikorsky Aircraft, where it was applied to failure analysis of helicopter flex beam. We are also using our methodology to investigate the applicability of various micromechanical failure criteria to failure prediction of composites under complex states of stress

Manuscript Submitted: Breitzman, T., Lipton, R. and Iarve, E. "Local Field Assessment Inside Multiscale Composite Architectures", SIAM Journal on Multiscale Analysis and Simulation.

Presentations made:

DISTRIBUTION STATEMENT A

Approved for Public Release
Distribution Unlimited

Lipton, R., Breitzman, T., and Larve, E. "Strength Assessment in Microstructured Materials, 7th World Congress on Computational Mechanics, Los Angeles, Ca , July, 2006

Lipton, R., Breitzman, T., and Larve, E. "Strength Assessment in Microstructured Materials, Gordon Research Conference, Thin Film & Small Scale Mechanical Behavior July 30 - August 4, 2006 Colby College Waterville, ME, August, 2006

Breitzman, T., Cook, B.M., G. Schoeppner and Larve, E. "Failure Prediction in a Uniaxially Loaded Composite Scarf Repair," ICMECE, Chicago IL, Nov. 5-11, 2006

Awards:

Endel V. Larve, 2006-2007 Wohlleben/Hochwalt Outstanding Professional Research Award, University Of Dayton.

Personnel

Principal Investigator- Dr. Endel V. Larve, UDRI

Co Principal Investigator- Prof. Robert Lipton, LSU (no direct charge to the grant)

Researcher – Sandeep Chellapilla, UDRI (FY-2004)

Researcher – Dr. Timothy Breitzman, AFRL (has worked on the grant while at LSU and UDRI)

EXECUTIVE SUMMARY

TASK 1. RVE models for fiber reinforced composite laminates were developed and verified to provide accurate prediction of effective mechanical and thermal expansion coefficients as a function of fiber volume fraction and constitutive properties of fiber and matrix. Anisotropy of the carbon fiber was taken into account. The quintessential part of the task was to demonstrate the accuracy of application of the simply coupled scales approximation (SCSA) at the locations where the microstructure periodicity conditions were not satisfied such as near free edges as well as interfaces between plies with different fiber orientation. To provide such estimates, fully three-dimensional models of cross ply laminate section with explicit modeling of fiber and matrix were built. Figure 1 illustrates these 3-D models. The directions of the coordinate axis with the origin in the lower left corner and the z –axis running in the vertical direction are shown in Figure 1 as well. The width of the model in the y-direction is equal to one unit cell size l_0 . The boundary conditions were applied as follows. At the x=constant facial surfaces periodicity conditions were applied along with 1% tensile strain loading in the x-direction. A displacement condition $u_z=0$ was applied at the surface $z=0$ and $u_y=0$ at the surface $y=10l_0$ so that the 3-D model corresponds to a quarter model of an infinitely long (in the x-direction) 3 ply laminate.

(a)

(b)

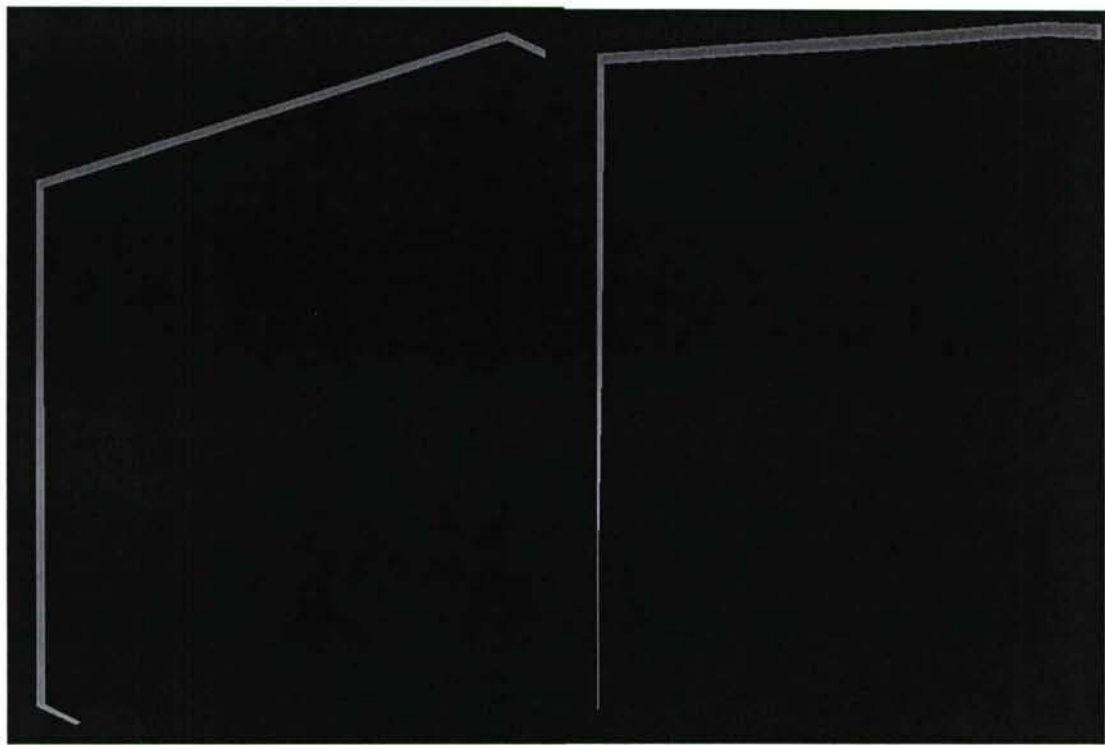


FIGURE 1. 3-D micromechanical models of (a) unidirectional/matrix laminate and (b) cross-ply laminates.

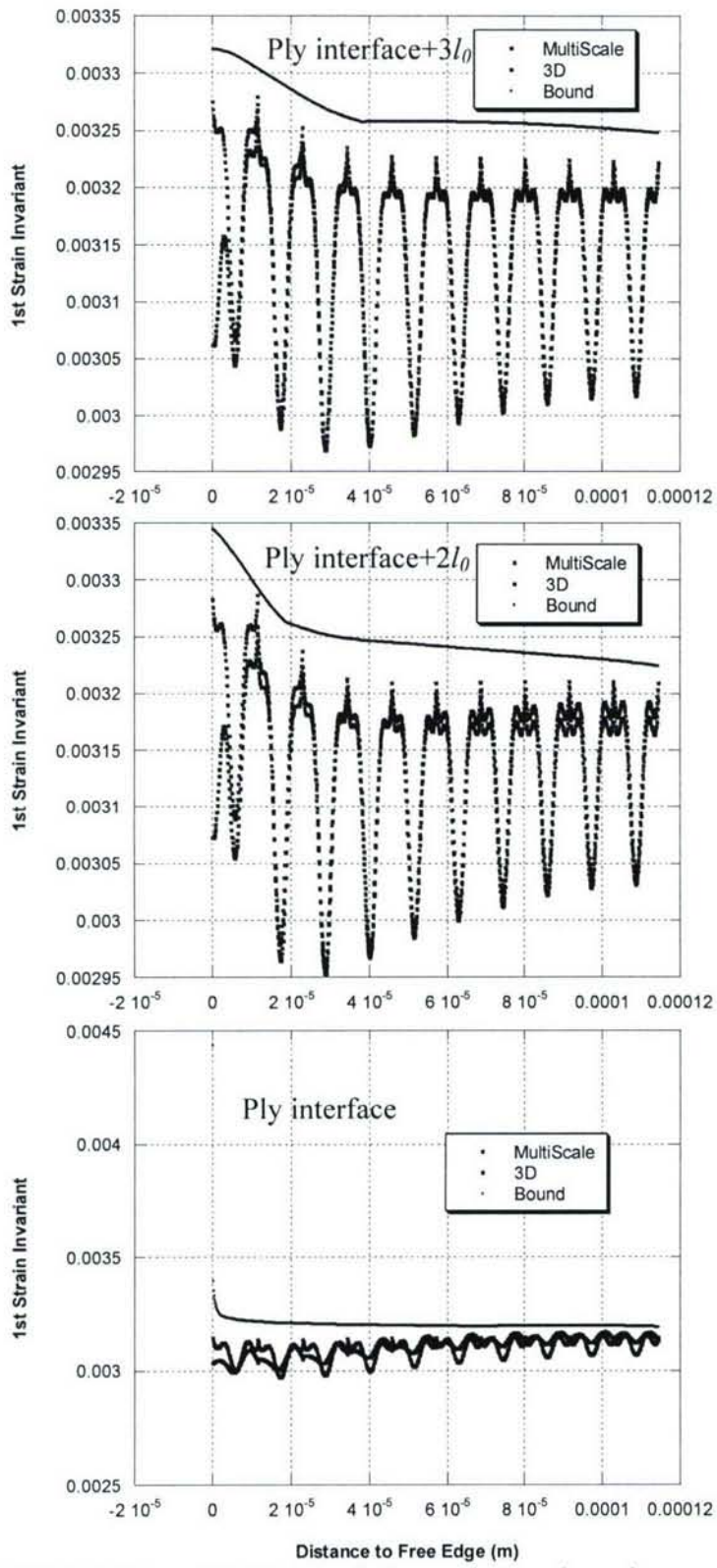


FIGURE 2. 3-D model, SCSA solution and stress bound comparison on fiber row interfaces

The number of unit cells modeled was determined by trial and error by increasing it until we had enough cells in the ply to achieve a good agreement between the micro level stresses predicted by SCSA and the full 3-D model in the internal cells. We focused on evaluation of the first and second invariants of the strain tensor, which we plan to apply for failure prediction as proposed in [6]. The results shown in Figure 2 pertain to the case of unidirectional/matrix ply laminate (Figure 1.a). Distribution of the first invariant of the strain tensor as a function of the distance from the free edge (y -coordinate) is shown at three different horizontal surfaces at $z=0$, $2l_0$, $3l_0$. In the middle of the top ply and away from the free edge, Figure 2.a, the results obtained by using the 3-D model and SCSA coincide. Apparently, the point values of the strain invariants obtained by SCSA are very accurate already for the third unit cell away from the free edge. The bound, which appears to over estimate the micro stress actually accounts for the strain concentrations on the fiber perimeter, which can also be seen on the 3-D solution if plotted around the fibers. Overall, the multiscale analysis results at the ply interface significantly overestimate the actual values of the micro field parameters.

The parametric studies in $[0/90]_s$ laminates revealed a less satisfying situation.

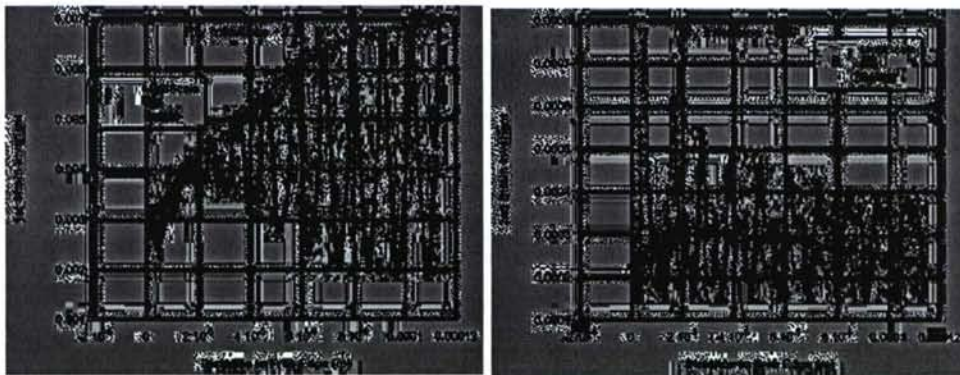


FIGURE 3. Free edge problem statement (a). First strain invariant as a function of distance from the hole edge 2.5 fiber rows above interface, and (b) the second strain invariant at the interface.

The distribution of the first and second strain invariants in the $[0/90]_s$ laminate loaded in tension in the 0^0 -direction is shown in Figure 3. The distributions are plotted for the fully 3D explicit solution modeling each fiber, for the multi scale simply-coupled scales approximation (SCSA) solution and the bound. It can be seen on Figure 3.a that the explicit and multiscale solution are in good agreement, even as close as 2.5 fiber diameters from the interface. However, at the interface, Figure 3.b, the multiscale solution and the bound greatly underestimate the amplitude of micro-strain distribution resulting from exact solution.

A key achievement of the work is the development of the rigorous homogenization framework based on special interface RVE, shown in Figure 4.a. The results obtained by using the multiscale

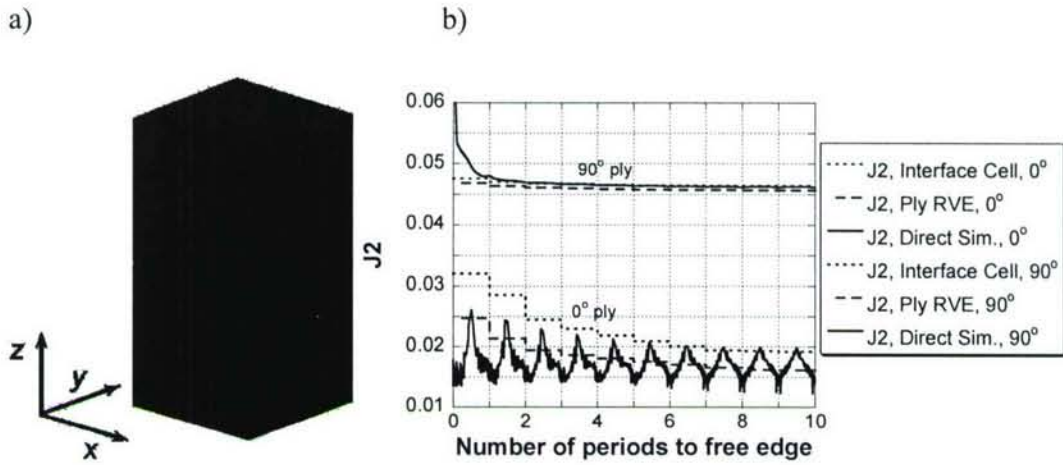


FIGURE 4. Interface RVE (a). The second strain invariant at the interface as a function of the distance from the free edge(b).

solution based on periodic (dashed line) and interface RVE (dotted line) are compared with the explicit 3D 60 fiber model (Figure 1b), and are displayed on Figure 4b. As it can be seen the periodic RVE based solution significantly underpredicts the upper bound of J_2 (second invariant of the strain tensor in the matrix phase) at the interface, whereas the estimate provided by the interface RVE based solution is much more realistic. These results are described in the manuscript, which we submitted to SIAM Journal on Multiscale Analysis.

TASK 2.

2.1 Free edge delamination. A fully 3-D ply level model of special dog bone shaped laminated composite specimen, shown in Figure 5, was developed according

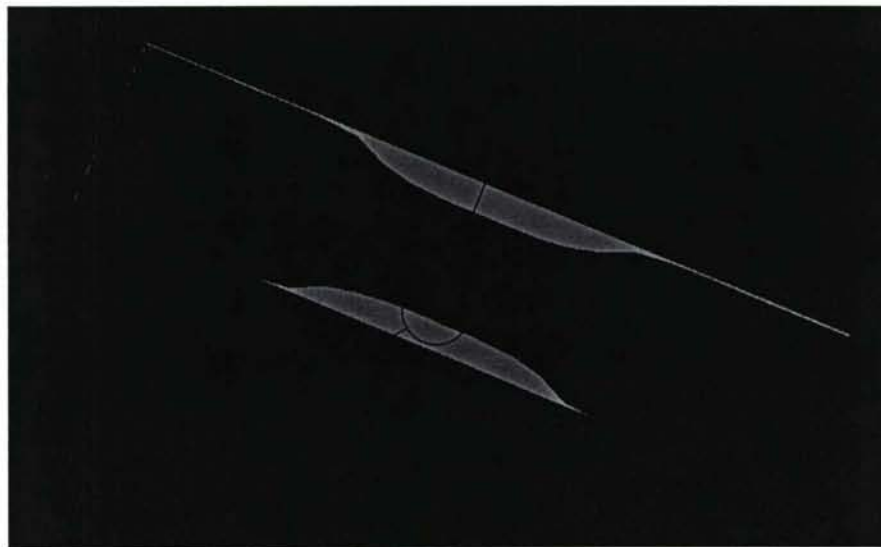
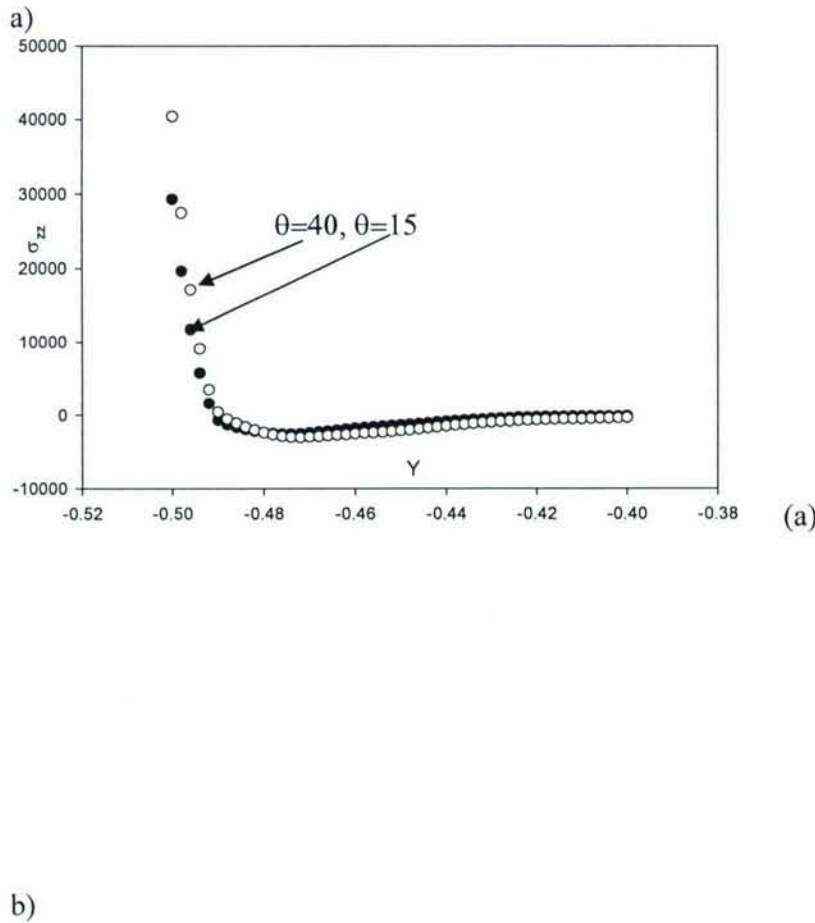


FIGURE 5. Schematics of the instrumented dog bone type specimen for delamination onset study.

to specifications [7] to prediction delamination initiation loads under axial tension loading. Two levels of analysis are considered for failure prediction, ply stress based failure criterion and micro-level failure criterion.

A comparison of ply level stress distributions in laminates with various layups is shown on Figure 6. The ply orientations in the laminates were $[0/-\theta/0/-\theta/90]_s$ for $\theta=15^\circ, 20^\circ, 25^\circ, 30^\circ, 35^\circ$ and 40° . The coordinate direction and origin are shown in Figure 5. Tensile loading is applied in the x-direction. According to the experimental study, the delamination initiation load for the laminates decreased by increasing θ . We examined the $x=0$ cross section of the laminate, which is in the gage section, where the delamination onset is monitored. Figure 6 shows the distribution of transverse normal and shear stress components σ_{zz} and σ_{yz} at the surfaces where they exhibited the maximum values, which were the midsurface and $0/-\theta$ surface for two laminates with $\theta=15^\circ$ and $\theta=40^\circ$.



(a)

b)

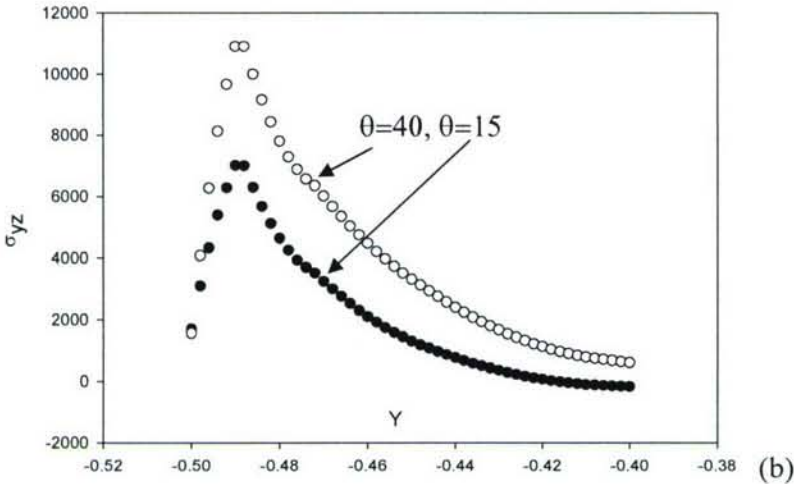


FIGURE 6. Stress component comparison of the ply level solution between laminates with $\theta=40^0$ (open markers) and $\theta=15^0$ laminates: (a) normal σ_{zz} stress at the mid-surface, $z=0$ and (b) transverse shear stress σ_{yz} at the $\theta/-\theta$ interface (b).

Both laminates are loaded with the same average strain. As seen in Figure 6 it is the transverse normal stress σ_{zz} which dominated over the shear stress magnitude in both laminates and its level in the $\theta=40^0$ laminate is higher near the free edge than in the $\theta=15^0$ laminate. This correlated well with the experimental data showing higher delamination initiation loads in the $\theta=15^0$ plies.

Multiscale analysis solution and calculated bounds for the first and second invariants of the strain tensor in the matrix phase are shown on Figure 7. In the example at hand we are less interested in fiber characteristics, since the initial failure mode is matrix cracking and delamination. Figure 7 displays the values of the first and second invariants of the strain tensor calculated at the midsurface in the $x=0$ cross section as a function of distance from the hole edge. Figure 7.a displays results obtained by using ply level analysis and Figure 7.b results obtained by using SCSA for the two laminates. In this case both solutions yield qualitatively similar results. Significantly larger values of the micro level stress bounds reflect the amplitude of the strain oscillation in the unit cell.

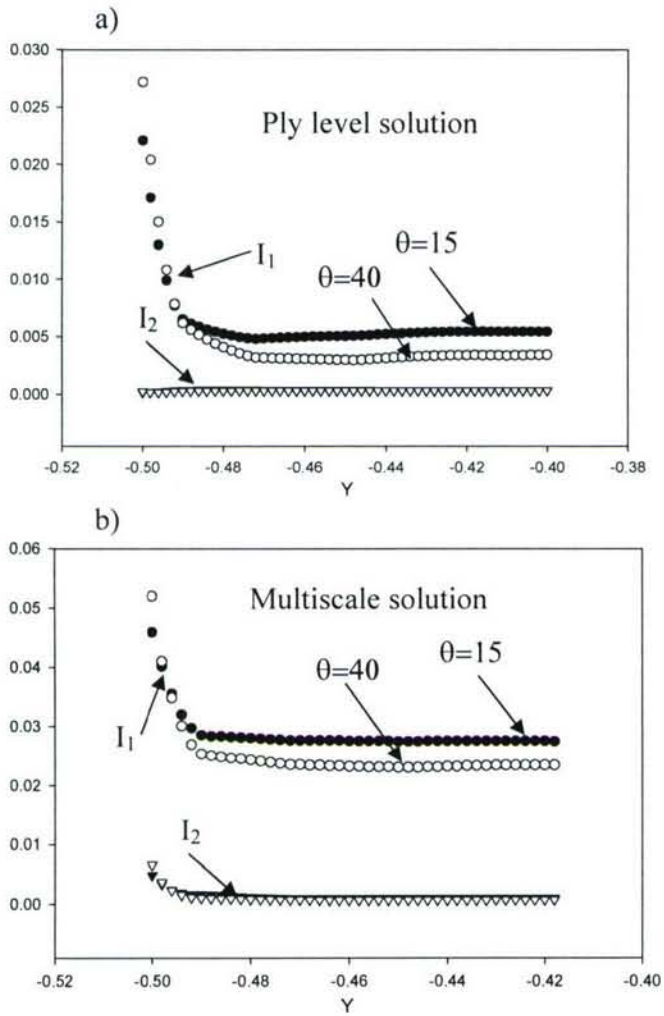


Figure 7. Comparison of the distributions of strain tensor invariants predicted in the matrix phase at the midsurface at $x=0$ as a function of distance from the free edge by using the ply level solution (a) and (b) the bounds of strain tensor invariants predicted by SCSA.

2.2. Normal open-hole. In this task, we compared the distribution of the level sets of matrix phase strain invariants calculated by using the multiscale solution and the level sets of the strain invariants calculated from the macro level strains. We also compared the normalized matrix phase strain invariants calculated by using the multiscale solution and the level sets of normalized macro-level stresses and their combinations. Such a comparison is motivated by the existing approach to failure prediction in composite laminates. Thus, the failure criteria applied on the micro level represent the Strain Invariant Failure Theory (SIFT) [6] and consist of the first and second invariants of the strain tensor. On the ply level, however, the most common failure criteria are applied in the stress space. We have calibrated both failure criteria with the same experimental values.

Comparison of invariants of the homogenized strain field to those of the macro level strain invariants. The first invariant bound and second invariant bound will be denoted $\mathcal{L}^M(e(u^0))$ and $\Pi^M(e(u^0))$, respectively. A 0° unidirectional, 4 in. x 1 in. rectangular plate with a 0.25 in. diameter open circular hole was considered. Ply thickness was 0.005 in. A 1% tension strain in the x -direction was applied as a displacement condition ($u_x = 0.04$) on the surface $x = 2$. In addition, the y -displacement was restricted on the surface $x = 2$. Similarly, the x -displacement and y -displacement were restricted on the surface $x = -2$. Midplane symmetry was provided for the laminate by the boundary condition $u_z = 0$ on the surface $z = 0$. Thus the results correspond to a 2-ply model.

Figure 8(a) and 8(b) display the level sets of the second invariant of the homogenized strain field and the bounds from the multiscale solution $\Pi^M(e(u^0))$, respectively. Figure 8 also suggests that the actual strain within the composite can be much larger than the state predicted by the homogenized strain field.

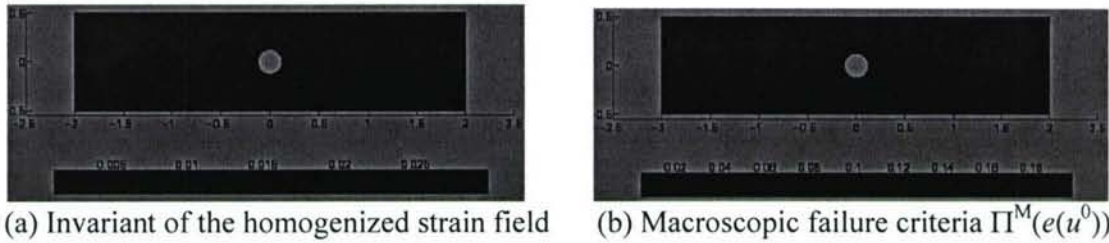


FIGURE 8: Second strain invariant comparison for unidirectional 0° laminate

Effect of thermal prestress. The model for the thermal prestress problem was identical to the model of the previous problem, except that we used a 4-ply laminate (the z -symmetry condition corresponds to an 8-ply symmetric laminate). Each ply in the laminate had a thickness of 0.005 in., and thus the 8-ply specimen was 0.04 in. thick in the z -direction. The 8-ply laminate was an IM7/977-3 [0/45/-45/90]_s composite. The symmetry plane was the surface $z = 0$. The strain invariant bounds in the matrix phase were computed at four z -heights in the model, corresponding to the middle (with respect to z) of each ply. The first strain invariant in the 45° ply is shown in Figure 9. The prestress appears to increase the invariant value by one order of magnitude on nearly the entire ply. This trend is representative of the prestress effects in the 0° and $\pm 45^\circ$ plies. The prestress did increase the first invariant value for the 90° ply, but by only a few tenths.

The values of the bounds for the second $\Pi^M(e(u^0))$ in the 45° ply are displayed in Figure 10. It is again clear from the figures that the prestress increases the second invariant values on nearly the entire plate. The prestress does not, however, appear to significantly increase the maximum of the second invariant inside the ply. It is seen that the prestress increases the volume of the sets experiencing the higher strain states. This volume can be crucial in failure predictions, and thus its increase is significant. It is important to note that second invariant values in the $\pm 45^\circ$ plies are about twice as large as the values in the 0° and 90° plies. The off-axis fiber orientation angles clearly experience larger shear strains.

It is important to note that the largest strains in each ply are concentrated very near the hole edge. Hence contours approaching these extreme values are not visible in these figures. The invariant contours plotted show the general trends of the invariants in each ply, but do not represent the extreme invariant values that occur. For the first invariant, the largest level-line plotted in each figure is roughly 50% of the maximum invariant in the ply. For the second invariant, the largest level-line shown in each set of figures is about 20% of the maximum invariant in the ply.

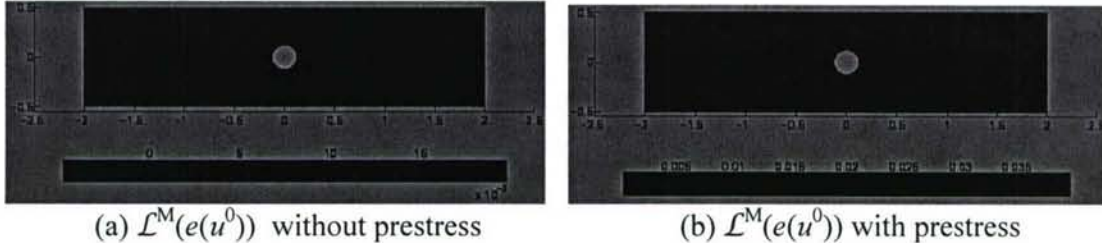


FIGURE 9: Macroscopic failure criteria $\mathcal{L}^M(e(u^0))$ in the $+45^\circ$ ply

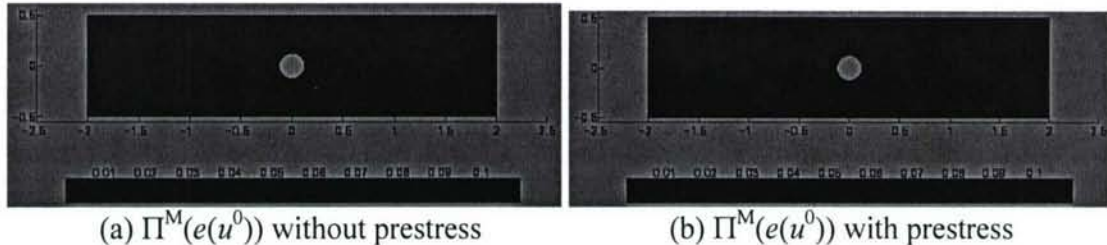


FIGURE 10: Macroscopic failure criteria $\Pi^M(e(u^0))$ in the $+45^\circ$ ply

Comparison of cubic RVE and hexagonal RVE. We created a hexagonal unit cell model. Figure 5 shows a schematic of the cubic and hexagonal unit cell models, respectively. The macroscopic computer model for this problem was an 8-ply, symmetric laminate with an open hole, and was identical in dimension and loading to the model for the previous problem. Data was taken with and without prestress, and the bounds of the strain invariants were computed at the same locations as the previous problem.

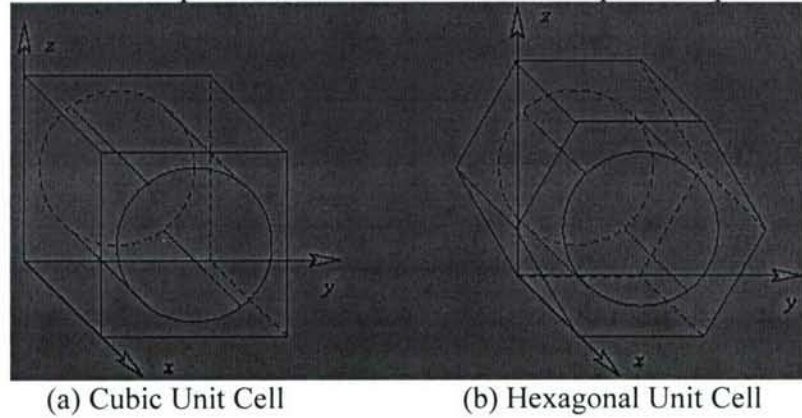


FIGURE 11: Schematic RVE models of two fiber reinforced geometries

Figure 12 shows the first invariant bounds $\mathcal{L}^M(e(u^0))$ with and without prestress. The figure suggests once again that the prestress increases the maximum value of the macroscopic failure criteria, as well as increasing its value on the entire plate. Comparing Figure 9 and Figure 12, it is also evident that the strain state is smaller when the microstructure is hexagonally periodic.

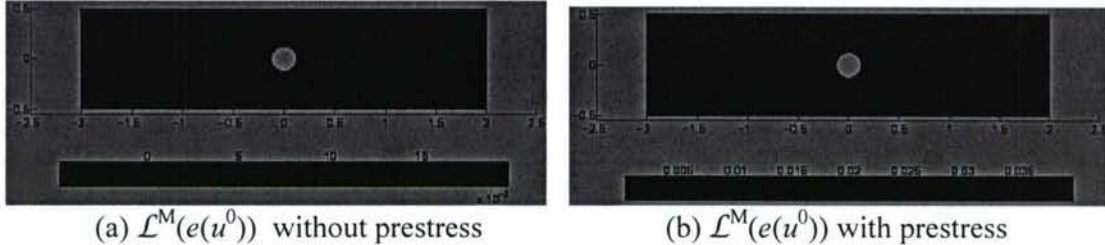


FIGURE 12: Bounds for the first strain invariant $\mathcal{L}^M(e(u^0))$ in the $+45^\circ$ ply

We note here that the color scales are the same for Figure 9 and Figure 12, as well as for Figure 10 and Figure 13. Thus the corresponding figures for the cubic RVE and the hexagonal RVE can be compared directly by observing the color. Figure 13 plots second strain invariant bound $\Pi^M(e(u^0))$ with and without prestress. Once again, the macroscopic failure criteria values calculated using the hexagonal RVE were less than the values calculated using the cubic RVE.

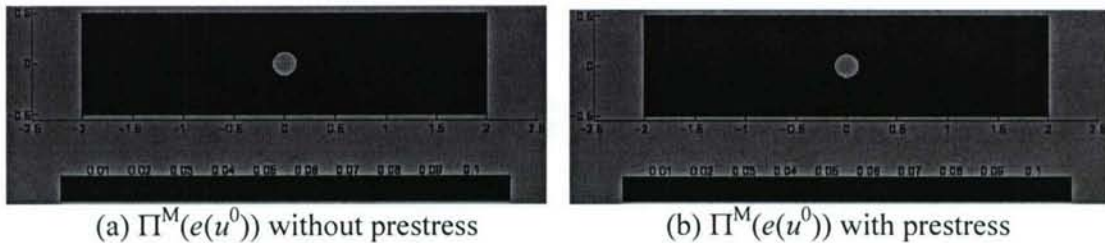


FIGURE 13: The bound for the second strain invariant $\Pi^M(e(u^0))$ in the $+45^\circ$ ply

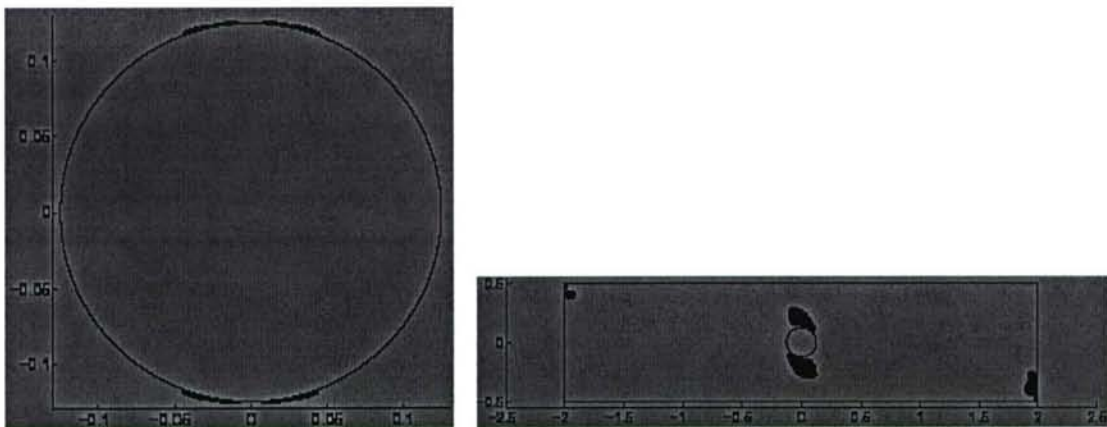
Failure analysis of a symmetric laminate with an open hole. We compared the normalized bounds of the matrix phase strain invariants with the normalized macro-level stress values and/or their combinations. Experimental strength data were used to back-calculate critical strain invariant values for the matrix phase of the composite. These critical values were used to normalize the strain invariant bounds. Hashin criteria and maximum stress criteria were applied to the ply level (homogenized) stresses. The over-stressed (over-strained) zone is the volume of the composite in which the value of the failure criteria meets or exceeds any of the critical strength parameters (indicated by yellow in Figures 15 – 19).

The computer model for this experiment was identical in dimension to the model of the previous two experiments. The loading, however, was reduced. Since complete

loss of load carrying capacity typically occurs between 0.6% strain and 0.7% strain, we computed over-stressed zones at 0.3% and 0.6% uniaxial tension (applied via displacement on the surface $x = 2$). All other boundary conditions were the same as in the prior experiments.

Figures 14, 15, and 16 display the overstressed zones for the phase strain invariant, Hashin failure criteria, and maximum stress failure criteria, respectively at 0.3% tension strain loading. At such a small loading, the 0° ply has very small overstressed zones just at the hole surface. The 45° ply shows moderately small over-stressed zones protruding from the hole surface out toward the ply edge. The -45° ply (not shown) was similar to the 45° ply, and the 90° ply (also not shown) was almost completely overstressed at just 0.3% strain. The three failure theories agree quite well on the location and size of the over-stressed zones. Moreover, the theories appear to agree on the failure mode. The dashed-line boundary around the macroscopic failure criteria overstrained zone (Figure 14(a)) indicates shear failure. The solid-line boundary around the Hashin overstressed zone (Figure 13(a)) indicates failure via a quadratic combination of transverse tension and in-plane shear forces. The boundary around the maximum stress over-stressed zone (Figure 14(a)) indicates failure by the in-plane shear force. Thus the results suggest that the three theories agree that the shear forces will initiate failure at the hole edge in the 0° ply.

Figures 17, 18, and 19 visualize the over-stressed zones for the micro level strain bounds, Hashin failure criteria, and max stress failure criteria, respectively at 0.6% tension strain loading. The 90° and $\pm 45^\circ$ plies all have large over-stressed zones (only $+45^\circ$ ply is shown). The small overstressed zones very near the hole edge in the 0° ply are the shear overstressed zones seen at 0.3% strain. These shear stresses near the hole edge produce the characteristic cracks running parallel to the fibers in the 0° ply. The slightly larger overstressed zones in the 0° ply appear to be transverse tension failure. These overstressed zones are believed to be an effect of the ply stacking sequence. Once again, the micro-level strain invariants based failure criteria appear to be consistent with the predictions of the Hashin failure criteria and the maximum stress failure criteria. In addition to the three different failure criteria being in agreement on the size and location of the overstressed zones, they also once again appear to agree on the failure mode in each case.



(a) 0° Ply

(b) $+45^\circ$ Ply

FIGURE 14: Micro level second strain invariant overstrained zone at 0.3% strain

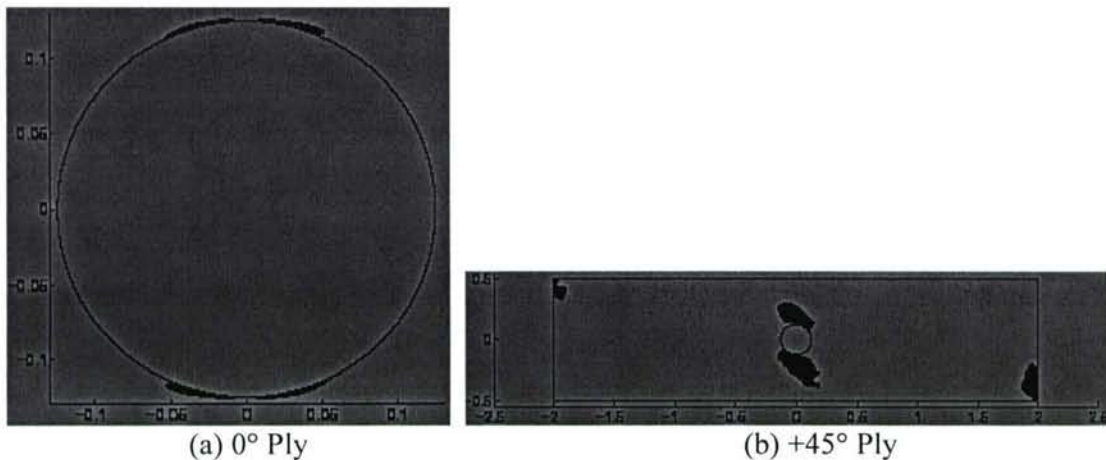


FIGURE 15: Hashin failure criteria overstressed zone at 0.3% strain

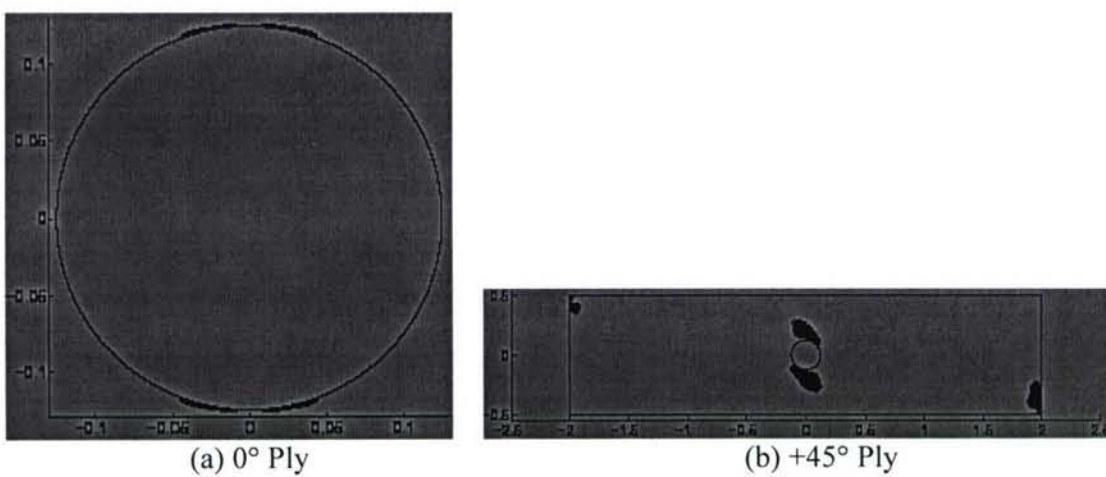


FIGURE 16: Maximum stress failure criteria overstressed zone at 0.3% strain



FIGURE 17: Micro-level second invariant overstrained zone at 0.6% strain



FIGURE 18: Hashin failure criteria overstressed zone at 0.6% strain



FIGURE 19: Maximum stress failure criteria overstressed zone at 0.6% strain

TASK 3. In this task we tried to understand the failure sequence of the composite scarf repair patch and construct a meaningful goal function for strength retention optimization. The main development in this task was to model nonlinear deformation and failure in the adhesive. The deformation of the composite and the patch was modeled with less detail on ply level. We heavily utilized experimental data obtained by Capt. B.M. Cook [8], which included fabrication and testing of the scarf repair as shown on Figure 20.



FIGURE 20. Experimental setup for tensile testing (a) and a plane view of the failed scarf repaired specimen (b).

The key finding in this task was that modeling of the failure of the adhesive in the nonlinear regime is crucial to predicting the strength of the repair. We found that despite

the low stiffness the adhesive transfers enough load in the elastic regime to practically remove the stress concentration due to scarfing and patching thus leading to 95% strength retention prediction. It is the adhesive failure that drastically increases the stress concentration in the parent panel and leads to premature failure. Spline approximation based 3D ply level analysis was used for failure prediction. The plate, adhesive and the repair patch models are shown on Figure 21.

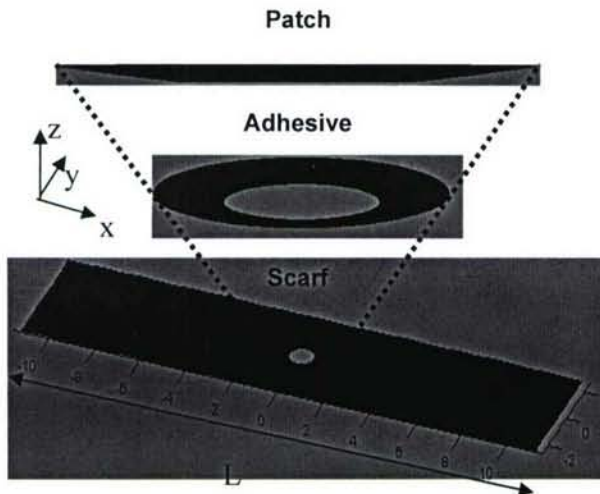


Figure 21. Computational model for the scarfed plate, patch and adhesive.

A nonlinear elastic model was utilized to model the adhesive. At the same time the fiber failure in the scarfed panel was predicted by using the critical failure volume (CFV) method recently proposed in [9-10]. The average applied load for fiber failure was predicted at each load level characterized by a state of delamination in the adhesive/scarfed panel interface. Initially, the stress distribution in the repaired panel is uniform and the fiber failure stress predicted is identical to that of virgin laminate. The increase of the applied load leads to initiation and growth of the delamination between the repair patch and the plate. The stress distribution in the patch becomes nonuniform with the stress concentration typical of open hole composites. At some applied load the average predicted fiber failure load and the applied load become equal. This load value is considered the failure load for the repaired panel.

The unidirectional properties of the IM6/3501-6 material were as follows: $E_{11}=175.27\text{Gpa}$, $E_{22}=E_{33}=9.79\text{Gpa}$, $v_{13}=v_{31}=0.33$, $v_{23}=0.49$, $G_{12}=G_{13}=5.51\text{Gpa}$ and $G_{23}=2.96\text{Gpa}$, with the coefficient of thermal expansion of $\alpha_{11}=4.10^{-6}\text{C}^0$ and $\alpha_{22}=32.10^{-6}\text{C}^0$. The Weibull parameters for the strength in the fiber direction were equal to $X_t=2.06\text{Gpa}$, $V_0=1638.7\text{mm}^3$ and $\alpha=40$. The value of the Weibull modulus was taken from Wisnom et al. [11]. The $l_{min}=0.266\text{mm}$ was calculated according to reference [9-10]. The initial elastic properties of the adhesive were $E=3.1\text{Gpa}$, $v=0.38$ and the thermal expansion coefficient was $\alpha=0.710^{-6}\text{C}^0$. The ply and adhesive thickness were $h=0.13\text{mm}$. The nonlinear shear deformation curve $\tau(\gamma)$ for the FM-300M adhesive was provided by

Structural Integrity Branch of the Air Force Research Laboratory's Materials and Manufacturing Directorate [12] and is shown in Figure 21. Three-dimensional nonlinear deformation of the adhesive was described by assuming nonlinear elasticity with constant Poisson ratio and shear modulus equal to $G = \Gamma(2/\sqrt{3} \varepsilon_{vm})$, where ε_{vm} – is Von-Mises strain, where $G(\gamma) = d\tau(\gamma)/d\gamma$. The temperature change $\Delta T = -155^{\circ}\text{C}$.

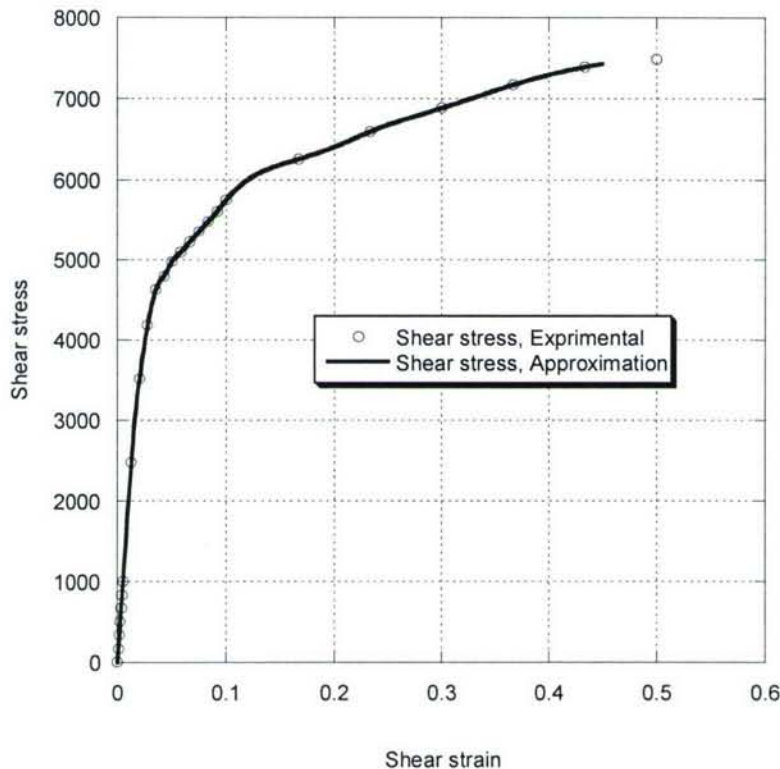


Figure 21. Nonlinear shear deformation curve of the for the FM-300M adhesive.

At low loads prior to the adhesive failure the stress field in the scarfed panel is quite uniform, as shown on the Figure 22. No stress concentration typical of an open hole is present. The average fiber failure load is predicted equal to that of virgin panels.



Figure 22. Normal σ_{xx} stress distribution (a) in the adhesive and (b) the scarfed plate prior to any delamination on the adhesive/panel interface

In the case of scarfed open hole panels a severe stress concentration typical of an open hole exists, Figure 23.a. The strength of such panels is about 1/3 of the virgin panels and is predicted accurately by using the CFV method [9-10]. Thus the strength of the repair is determined by the adhesive failure and/or its nonlinear behavior. The stress distribution in the parent panel corresponding to partially failed adhesive is shown on Figure 23b. This stress concentration is less severe than in the case of open scarfed hole and the predicted strength values of the repaired panels are at the level of 2/3 of the initial virgin panel strength.



Figure 23. Normal σ_{xx} stress distribution in the scarfed and repaired panels. (a) Open scarfed hole and (b) partially delaminated adhesive at 90% of the scarf failure load.

Experimental data and predicted strength values for small and large size unnotched tensile coupons, as well as strength of scarfed open hole and scarfed repaired panels are shown on Figure 24. Significant reduction in experimentally measured strength of large virgin panels as compared to small coupons is attributed to grip failure of most large virgin specimens. Only 5% strength reduction due to volume increase is predicted theoretically. All unrepaired and repaired scarfed laminates exhibited brittle failure through the cavity, thus rendering the test data valid for comparison with theoretical predictions. The predicted strength values for both cases are close to those measured

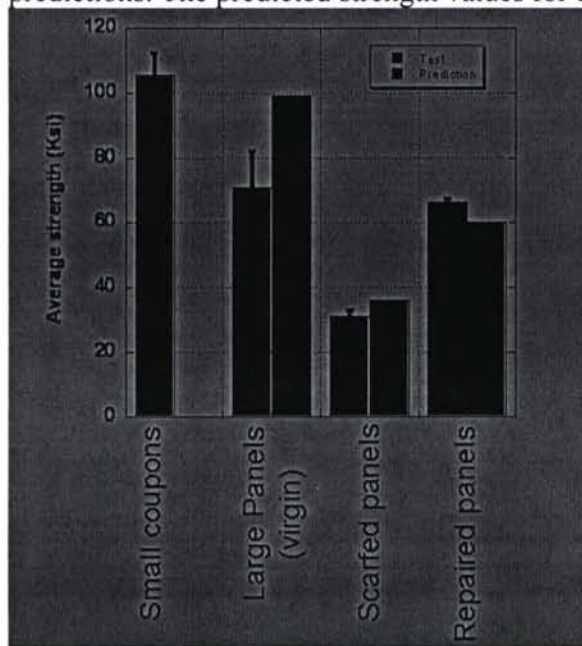


Figure 24. Experimental and numerical results

experimentally.

TASK 4. Development of an automated multiscale mechanism within the B-spline Approximation Method (BSAM) computer program was accomplished ahead of schedule and utilized to produce all results demonstrated in this report.

TASK 5.

In the course of the project, we have understood that our original vision of repair optimization based on elastic properties of adhesive was too simplistic. Indeed as seen from the previous task the repair strength is a direct function of the adhesive failure, which determines the load transfer between the repair patch and the parent laminate. An optimization algorithm which would be based on a repair strength as a goal function will be highly impractical, requiring nonlinear analysis at every optimization iteration and preventing the use of gradient methods [13] for optimization. These complications delayed our progress and required to propose alternative optimization ideas. The one we have selected for implementation is to minimize an elastic L_p norm of a stress invariant failure criteria in the adhesive. Such an approach is targeted to the delay of failure initiation in the adhesive. Although not completed, we have obtained encouraging results. Recall Figure 24, where the predicted strength of the repaired composite was at 60Ksi. This result was obtained for a traditional ply by ply replacement composition of the repair patch. After we switched two ply orientations, namely 0° and 90° inside this patch, we delayed the onset of adhesive failure to 65Ksi. We expect to further delay the adhesive failure by application of the optimization algorithm. These developments are being closely followed by the Structural Integrity Branch of the Air Force Research Laboratory's Materials and Manufacturing Directorate, which is presently conducting an experimental program to verify our findings.

CONCLUSIONS

1) We integrated the rigorous microlevel (fiber, matrix) stress bound estimates by using simply coupled scale analysis, with the spline approximation stress analysis tools - BSAM. A robust multiscale analysis framework was developed and applied within and beyond the scope of the present grant.

2) A key development was the extension of the stress bound estimates in heterogeneous materials with periodic microstructure to include regions of nonperiodic microstructure. Such regions included ply interfaces in fiber reinforced composite materials, which are present in all laminated composite structures. The improved accuracy of the multiscale analysis was verified by comparison with three-dimensional analysis of model cross ply composite laminate, where fibers were modeled explicitly.

3) The developed capabilities were applied to composite scarf repair optimization. Our analysis addressed, for the first time, the composition of the repair patch in addition to more conventional geometric parameters, such as scarf angle and repair depth. We found that altering the conventional ply by ply replacement schema of the repair patch does not lead to premature failure, but delays the failure of the adhesive and increases the

strength of the repaired composite. This work is coordinated with Structural Integrity Branch of the Air Force Research Laboratory's Materials and Manufacturing Directorate, which is presently executing an experimental program to verify our findings.

4) We have transitioned the periodic RVE based micromechanical failure criterion evaluation algorithm to Sikorsky Aircraft, where it was applied to failure analysis of a helicopter flex beam. We are also applying our methodology to investigate applicability of various micromechanical failure criteria to failure prediction of composites under complex states of stress.

REFERENCES

1. Lipton, R. (2003). "Assessment of the Local Stress State through Macroscopic Variables," *Philosophical Transactions of the Royal Society of London A*, 361, pp. 921--946.
2. Lipton, R. (2004)., "Stress Constrained G Closure and Relaxation of Structural Design Problems," *Quarterly of Applied Mathematics*, **62**, 295-321
3. Iarve, E. V. (1996). Spline Variational Three-Dimensional Stress Analysis of Laminated Composite Plates with Open Holes. *Int. J. of Solids and Structures* 33(14) (2095-2117).
4. Iarve, E. V. (1997). Three-Dimensional Stress Analysis in Laminated Composite Plates with Fasteners Based on the B-Spline Approximation. *Composites: Part A*, 28A (559-571).
5. Iarve, E. V., & N. J. Pagano., (2001). Singular Full-Field Stresses in Composite Laminates with Open Holes. *Int. J. Solids Structures* 38(1) (1-28).
6. Gosse, J.H. and Christensen, S. (2001) "Strain Invariant Failure Criteria for Polymers in Composite Material" AIAA-2001-1184, p.11.
7. Sandhu, R.S., Sendeckyj G.P., Schoeppner, G.A. and Papas, J.E. (1992) "Initiation and Prevention of Edge Delamination with and without Residual Stresses" Proceedings of 74th meeting of the Structures and Materials Panel AGARD, AGARD-CP-530, Patras, Greece, 27-28 May 1992
8. Cook, B.M, "Experimentation and Analysis of Composite Scarf Joint," M.S. Thesis, Air Force Institute of Technology, March 2005.
9. Iarve, E.V., Kim, R. and Mollenhauer, D. (2007) "Three-Dimensional Stress Analysis and Weibull Statistics Based Strength Prediction in Open Hole Composite Laminates" *Composite Part A*, **38**, 174-185 .
10. Iarve, E.V., Mollenhauer, D., Whitney, T. and Kim, R. (2006) "Strength Prediction in Composites with Stress Concentrations: Classical Weibull and Critical Failure Volume Methods with Micromechanical Considerations", *J. of Material Science*, **41**(20), pp. 6610-6622
11. Wisnom, M. R., B. Khan, B. Green, W. Jiang and S. R. Hallet (2005), "Specimen Size Effects on Tensile Strength and Failure Mechanisms of

Carbon/Epoxy Composites," *JNC14 Conference*, Compiegne, March 2005.

- 12. Bolan, B. (2007), "Personal communication"
- 13. Lipton, R. and Stuebner, M., (2006) "Inverse Homogenization and Design of Microstructure for Pointwise Stress Control", *Qrt. J. Mech. and Appl. Math.*, **59**, pp. 131-169.

University of Dayton Research Institute

Endel V. Iarve

**Micro-stress bound estimate enabled optimization of structural composite repair for
the next generation aircraft**

Final Report

FY04-06

Grant: FA0550-04-1-0142

ABSTRACT The completed effort integrated the rigorous microlevel (fiber, matrix, sizing) stress bound recently obtained by Lipton [1,2] under AFOSR sponsorship with the AFRL-developed ply level multibasis spline approximation stress analysis tools [3-5]. A robust multiscale analysis framework was developed and applied within and beyond the scope of the present grant. The developments included extension of the stress bound estimates in heterogeneous materials with periodic microstructure to include residual stress effects and, notably, regions of nonperiodic microstructure. Such regions included ply interfaces in fiber reinforced composite materials, which are present in all laminated composite structures. The improved accuracy of the multiscale analysis was verified by comparison with three-dimensional analysis of model cross ply composite laminate, where fibers were modeled explicitly. Our analysis capability for the first time addressed the composition of the repair patch of a composite scarf repair in addition to more conventional geometric parameters, such as scarf angle and repair depth. We found that altering the conventional ply by ply replacement schema of the repair patch does not lead to premature failure, but may delay the failure of the adhesive and increase the strength of the repaired composite. This work is well coordinated with the Materials Integrity Branch of the Air Force Research Laboratory's Materials and Manufacturing Directorate, which is presently executing an experimental program to verify our findings. We have transitioned the periodic RVE based micromechanical failure criterion evaluation algorithm to Sikorsky Aircraft, where it was applied to failure analysis of helicopter flex beam. We are also using our methodology to investigate the applicability of various micromechanical failure criteria to failure prediction of composites under complex states of stress

Manuscript Submitted: Breitzman, T., Lipton, R. and Iarve, E. "Local Field Assessment Inside Multiscale Composite Architectures", SIAM Journal on Multiscale Analysis and Simulation.

Presentations made:

Lipton, R., Breitzman, T., and Larve, E. "Strength Assessment in Microstructured Materials, 7th World Congress on Computational Mechanics, Los Angeles, Ca , July, 2006

Lipton, R., Breitzman, T., and Larve, E. "Strength Assessment in Microstructured Materials, Gordon Research Conference, Thin Film & Small Scale Mechanical Behavior July 30 - August 4, 2006 Colby College Waterville, ME, August, 2006

Breitzman, T., Cook, B.M., G. Schoeppner and Larve, E. "Failure Prediction in a Uniaxially Loaded Composite Scarf Repair," ICMECE, Chicago IL, Nov. 5-11, 2006

Awards:

Endel V. Larve, 2006-2007 Wohlleben/Hochwalt Outstanding Professional Research Award, University Of Dayton.

Personnel

Principal Investigator- Dr. Endel V. Larve, UDRI

Co Principal Investigator- Prof. Robert Lipton, LSU (no direct charge to the grant)

Researcher – Sandeep Chellapilla, UDRI (FY-2004)

Researcher – Dr. Timothy Breitzman, AFRL (has worked on the grant while at LSU and UDRI)

EXECUTIVE SUMMARY

TASK 1. RVE models for fiber reinforced composite laminates were developed and verified to provide accurate prediction of effective mechanical and thermal expansion coefficients as a function of fiber volume fraction and constitutive properties of fiber and matrix. Anisotropy of the carbon fiber was taken into account. The quintessential part of the task was to demonstrate the accuracy of application of the simply coupled scales approximation (SCSA) at the locations where the microstructure periodicity conditions were not satisfied such as near free edges as well as interfaces between plies with different fiber orientation. To provide such estimates, fully three-dimensional models of cross ply laminate section with explicit modeling of fiber and matrix were built. Figure 1 illustrates these 3-D models. The directions of the coordinate axis with the origin in the lower left corner and the z –axis running in the vertical direction are shown in Figure 1 as well. The width of the model in the y-direction is equal to one unit cell size l_0 . The boundary conditions were applied as follows. At the x=constant facial surfaces periodicity conditions were applied along with 1% tensile strain loading in the x-direction. A displacement condition $u_z=0$ was applied at the surface $z=0$ and $u_y=0$ at the surface $y=10l_0$ so that the 3-D model corresponds to a quarter model of an infinitely long (in the x-direction) 3 ply laminate.

(a)

(b)



FIGURE 1. 3-D micromechanical models of (a) unidirectional/matrix laminate and (b) cross-ply laminates.

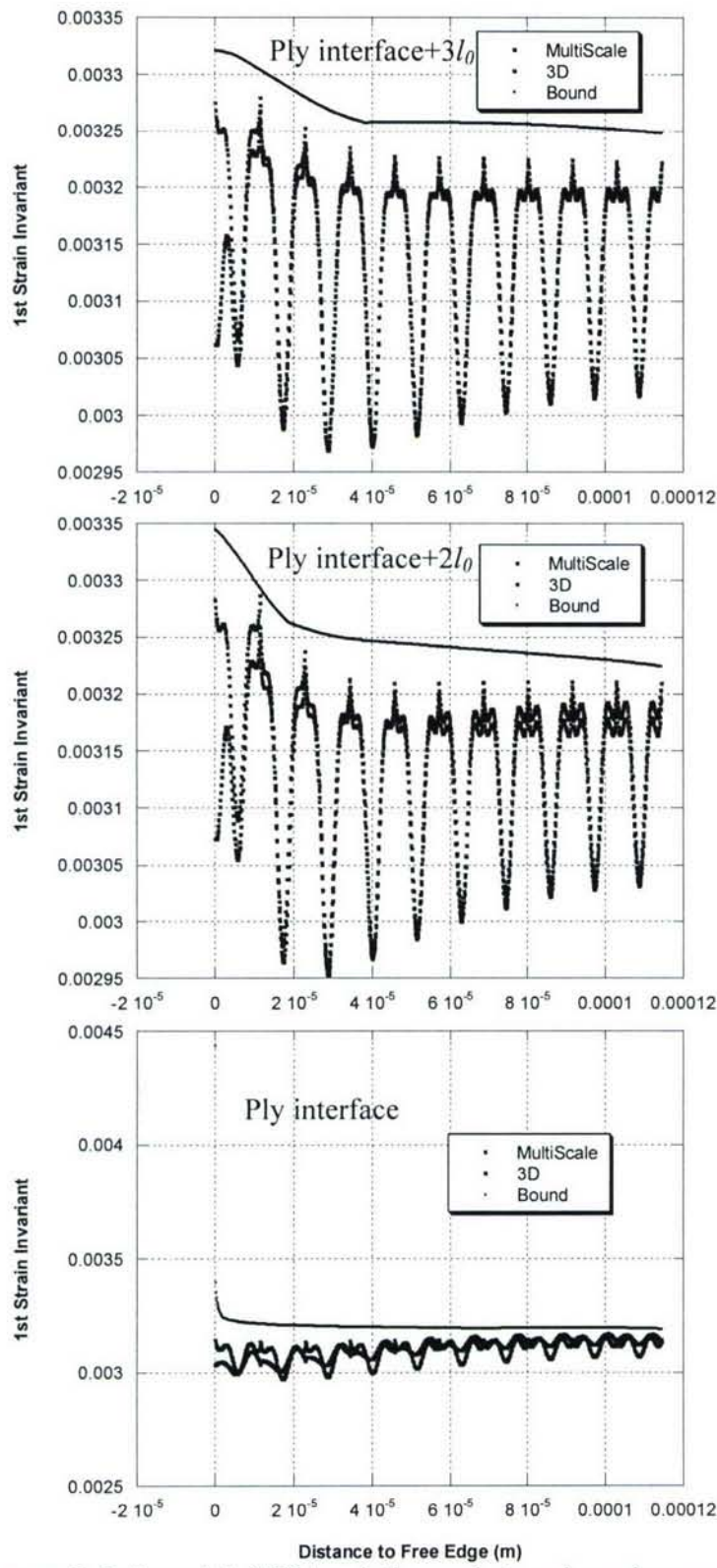


FIGURE 2. 3-D model, SCSA solution and stress bound comparison on fiber row interfaces

The number of unit cells modeled was determined by trial and error by increasing it until we had enough cells in the ply to achieve a good agreement between the micro level stresses predicted by SCSA and the full 3-D model in the internal cells. We focused on evaluation of the first and second invariants of the strain tensor, which we plan to apply for failure prediction as proposed in [6]. The results shown in Figure 2 pertain to the case of unidirectional/matrix ply laminate (Figure 1.a). Distribution of the first invariant of the strain tensor as a function of the distance from the free edge (y -coordinate) is shown at three different horizontal surfaces at $z=0, 2l_0, 3l_0$. In the middle of the top ply and away from the free edge, Figure 2.a, the results obtained by using the 3-D model and SCSA coincide. Apparently, the point values of the strain invariants obtained by SCSA are very accurate already for the third unit cell away from the free edge. The bound, which appears to over estimate the micro stress actually accounts for the strain concentrations on the fiber perimeter, which can also be seen on the 3-D solution if plotted around the fibers. Overall, the multiscale analysis results at the ply interface significantly overestimate the actual values of the micro field parameters.

The parametric studies in $[0/90]_s$ laminates revealed a less satisfying situation.

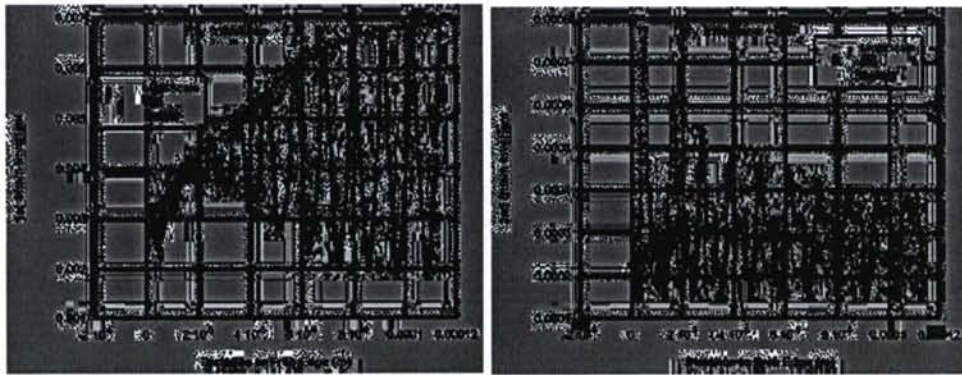


FIGURE 3. Free edge problem statement (a). First strain invariant as a function of distance from the hole edge 2.5 fiber rows above interface, and (b) the second strain invariant at the interface.

The distribution of the first and second strain invariants in the $[0/90]_s$ laminate loaded in tension in the 0^0 -direction is shown in Figure 3. The distributions are plotted for the fully 3D explicit solution modeling each fiber, for the multi scale simply-coupled scales approximation (SCSA) solution and the bound. It can be seen on Figure 3.a that the explicit and multiscale solution are in good agreement, even as close as 2.5 fiber diameters from the interface. However, at the interface, Figure 3.b, the multiscale solution and the bound greatly underestimate the amplitude of micro-strain distribution resulting from exact solution.

A key achievement of the work is the development of the rigorous homogenization framework based on special interface RVE, shown in Figure 4.a. The results obtained by using the multiscale

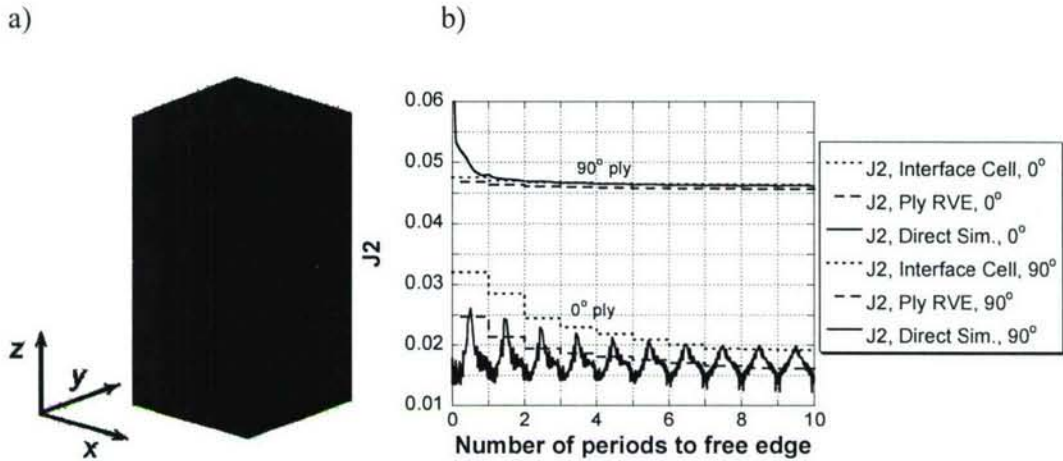


FIGURE 4. Interface RVE (a). The second strain invariant at the interface as a function of the distance from the free edge(b).

solution based on periodic (dashed line) and interface RVE (dotted line) are compared with the explicit 3D 60 fiber model (Figure 1b), and are displayed on Figure 4b. As it can be seen the periodic RVE based solution significantly underpredicts the upper bound of J_2 (second invariant of the strain tensor in the matrix phase) at the interface, whereas the estimate provided by the interface RVE based solution is much more realistic. These results are described in the manuscript, which we submitted to SIAM Journal on Multiscale Analysis.

TASK 2.

2.1 Free edge delamination. A fully 3-D ply level model of special dog bone shaped laminated composite specimen, shown in Figure 5, was developed according

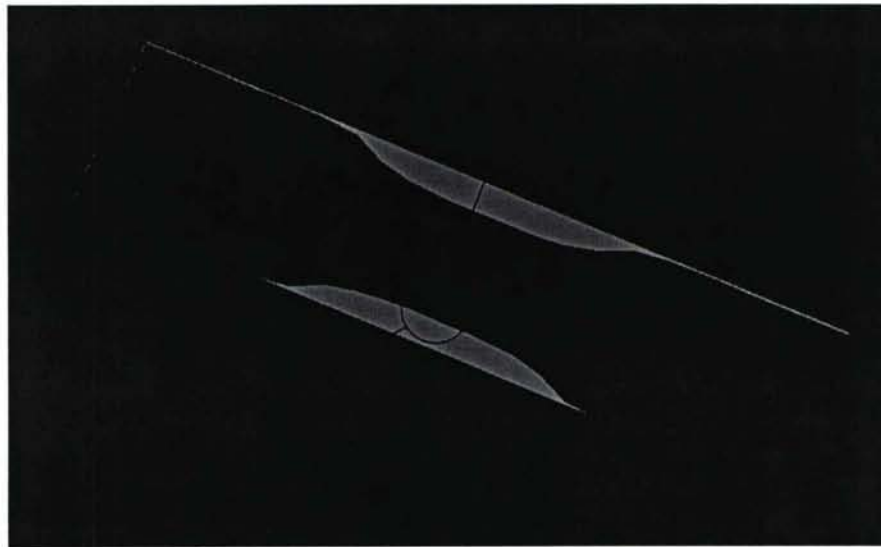
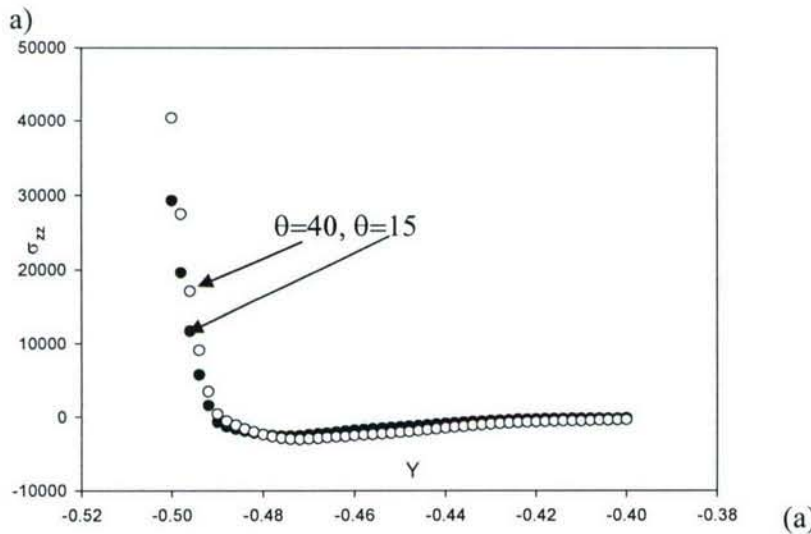


FIGURE 5. Schematics of the instrumented dog bone type specimen for delamination onset study.

to specifications [7] to predict delamination initiation loads under axial tension loading. Two levels of analysis are considered for failure prediction, ply stress based failure criterion and micro-level failure criterion.

A comparison of ply level stress distributions in laminates with various layups is shown on Figure 6. The ply orientations in the laminates were $[\theta/-\theta/\theta/-\theta/90]_s$ for $\theta=15^\circ, 20^\circ, 25^\circ, 30^\circ, 35^\circ$ and 40° . The coordinate direction and origin are shown in Figure 5. Tensile loading is applied in the x-direction. According to the experimental study, the delamination initiation load for the laminates decreased by increasing θ . We examined the $x=0$ cross section of the laminate, which is in the gage section, where the delamination onset is monitored. Figure 6 shows the distribution of transverse normal and shear stress components σ_{zz} and σ_{yz} at the surfaces where they exhibited the maximum values, which were the midsurface and $\theta/-\theta$ surface for two laminates with $\theta=15^\circ$ and $\theta=40^\circ$.



(a)

b)

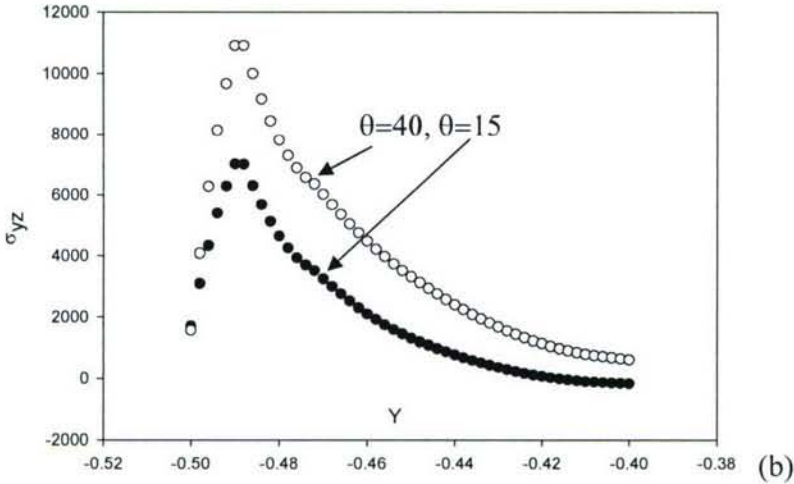


FIGURE 6. Stress component comparison of the ply level solution between laminates with $\theta=40^0$ (open markers) and $\theta=15^0$ laminates (filled markers): (a) normal σ_{zz} stress at the mid-surface, $z=0$ and (b) transverse shear stress σ_{yz} at the $\theta/-\theta$ interface (b).

Both laminates are loaded with the same average strain. As seen in Figure 6 it is the transverse normal stress σ_{zz} which dominated over the shear stress magnitude in both laminates and its level in the $\theta=40^0$ laminate is higher near the free edge than in the $\theta=15^0$ laminate. This correlated well with the experimental data showing higher delamination initiation loads in the $\theta=15^0$ plies.

Multiscale analysis solution and calculated bounds for the first and second invariants of the strain tensor in the matrix phase are shown on Figure 7. In the example at hand we are less interested in fiber characteristics, since the initial failure mode is matrix cracking and delamination. Figure 7 displays the values of the first and second invariants of the strain tensor calculated at the midsurface in the $x=0$ cross section as a function of distance from the hole edge. Figure 7.a displays results obtained by using ply level analysis and Figure 7.b results obtained by using SCSA for the two laminates. In this case both solutions yield qualitatively similar results. Significantly larger values of the micro level stress bounds reflect the amplitude of the strain oscillation in the unit cell.

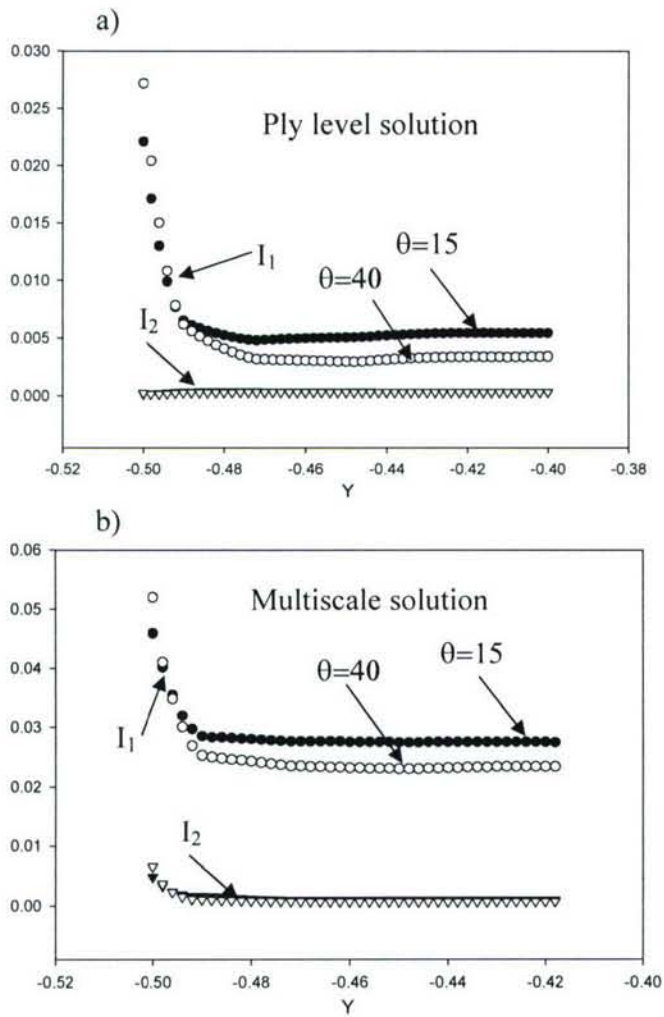


Figure 7. Comparison of the distributions of strain tensor invariants predicted in the matrix phase at the midsurface at $x=0$ as a function of distance from the free edge by using the ply level solution (a) and (b) the bounds of strain tensor invariants predicted by SCSA.

2.2. Normal open-hole. In this task, we compared the distribution of the level sets of matrix phase strain invariants calculated by using the multiscale solution and the level sets of the strain invariants calculated from the macro level strains. We also compared the normalized matrix phase strain invariants calculated by using the multiscale solution and the level sets of normalized macro-level stresses and their combinations. Such a comparison is motivated by the existing approach to failure prediction in composite laminates. Thus, the failure criteria applied on the micro level represent the Strain Invariant Failure Theory (SIFT) [6] and consist of the first and second invariants of the strain tensor. On the ply level, however, the most common failure criteria are applied in the stress space. We have calibrated both failure criteria with the same experimental values.

Comparison of invariants of the homogenized strain field to those of the macro level strain invariants. The first invariant bound and second invariant bound will be denoted $\mathcal{L}^M(e(u^0))$ and $\Pi^M(e(u^0))$, respectively. A 0° unidirectional, 4 in. x 1 in. rectangular plate with a 0.25 in. diameter open circular hole was considered. Ply thickness was 0.005 in. A 1% tension strain in the x -direction was applied as a displacement condition ($u_x = 0.04$) on the surface $x = 2$. In addition, the y -displacement was restricted on the surface $x = 2$. Similarly, the x -displacement and y -displacement were restricted on the surface $x = -2$. Midplane symmetry was provided for the laminate by the boundary condition $u_z = 0$ on the surface $z = 0$. Thus the results correspond to a 2-ply model.

Figure 8(a) and 8(b) display the level sets of the second invariant of the homogenized strain field and the bounds from the multiscale solution $\Pi^M(e(u^0))$, respectively. Figure 8 also suggests that the actual strain within the composite can be much larger than the state predicted by the homogenized strain field.

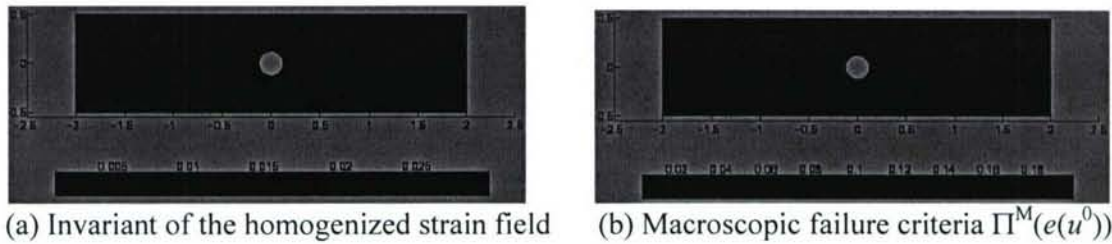


FIGURE 8: Second strain invariant comparison for unidirectional 0° laminate

Effect of thermal prestress. The model for the thermal prestress problem was identical to the model of the previous problem, except that we used a 4-ply laminate (the z -symmetry condition corresponds to an 8-ply symmetric laminate). Each ply in the laminate had a thickness of 0.005 in., and thus the 8-ply specimen was 0.04 in. thick in the z -direction. The 8-ply laminate was an IM7/977-3 [0/45/-45/90]_s composite. The symmetry plane was the surface $z = 0$. The strain invariant bounds in the matrix phase were computed at four z -heights in the model, corresponding to the middle (with respect to z) of each ply. The first strain invariant in the 45° ply is shown in Figure 9. The prestress appears to increase the invariant value by one order of magnitude on nearly the entire ply. This trend is representative of the prestress effects in the 0° and $\pm 45^\circ$ plies. The prestress did increase the first invariant value for the 90° ply, but by only a few tenths.

The values of the bounds for the second $\Pi^M(e(u^0))$ in the 45° ply are displayed in Figure 10. It is again clear from the figures that the prestress increases the second invariant values on nearly the entire plate. The prestress does not, however, appear to significantly increase the maximum of the second invariant inside the ply. It is seen that the prestress increases the volume of the sets experiencing the higher strain states. This volume can be crucial in failure predictions, and thus its increase is significant. It is important to note that second invariant values in the $\pm 45^\circ$ plies are about twice as large as the values in the 0° and 90° plies. The off-axis fiber orientation angles clearly experience larger shear strains.

It is important to note that the largest strains in each ply are concentrated very near the hole edge. Hence contours approaching these extreme values are not visible in these figures. The invariant contours plotted show the general trends of the invariants in each ply, but do not represent the extreme invariant values that occur. For the first invariant, the largest level-line plotted in each figure is roughly 50% of the maximum invariant in the ply. For the second invariant, the largest level-line shown in each set of figures is about 20% of the maximum invariant in the ply.

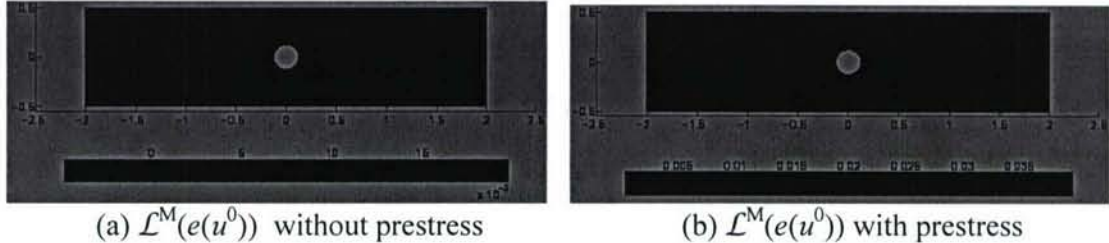


FIGURE 9: Macroscopic failure criteria $\mathcal{L}^M(e(u^0))$ in the $+45^\circ$ ply

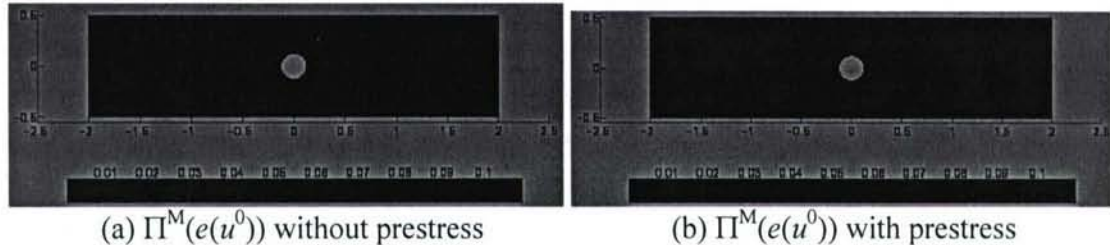


FIGURE 10: Macroscopic failure criteria $\Pi^M(e(u^0))$ in the $+45^\circ$ ply

Comparison of cubic RVE and hexagonal RVE. We created a hexagonal unit cell model. Figure 5 shows a schematic of the cubic and hexagonal unit cell models, respectively. The macroscopic computer model for this problem was an 8-ply, symmetric laminate with an open hole, and was identical in dimension and loading to the model for the previous problem. Data was taken with and without prestress, and the bounds of the strain invariants were computed at the same locations as the previous problem.

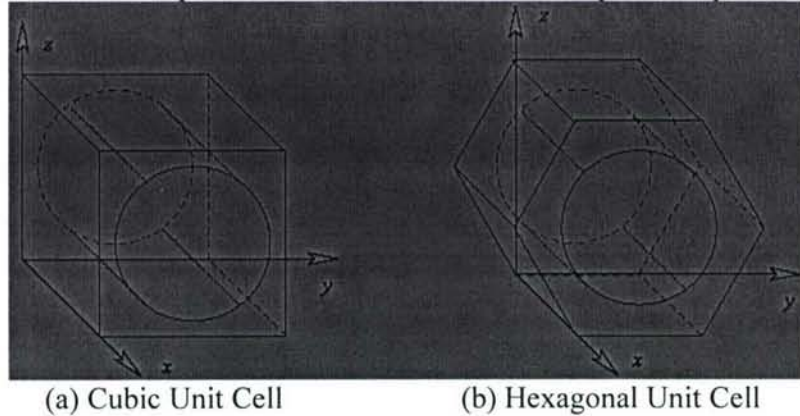


FIGURE 11: Schematic RVE models of two fiber reinforced geometries

Figure 12 shows the first invariant bounds $\mathcal{L}^M(e(u^0))$ with and without prestress. The figure suggests once again that the prestress increases the maximum value of the macroscopic failure criteria, as well as increasing its value on the entire plate. Comparing Figure 9 and Figure 12, it is also evident that the strain state is smaller when the microstructure is hexagonally periodic.

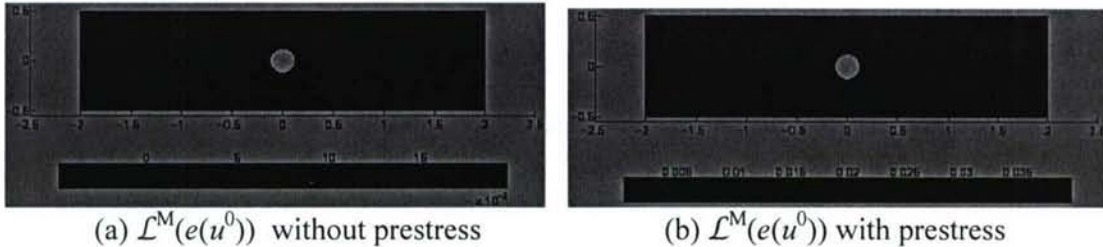


FIGURE 12: Bounds for the first strain invariant $\mathcal{L}^M(e(u^0))$ in the $+45^\circ$ ply

We note here that the color scales are the same for Figure 9 and Figure 12, as well as for Figure 10 and Figure 13. Thus the corresponding figures for the cubic RVE and the hexagonal RVE can be compared directly by observing the color. Figure 13 plots second strain invariant bound $\Pi^M(e(u^0))$ with and without prestress. Once again, the macroscopic failure criteria values calculated using the hexagonal RVE were less than the values calculated using the cubic RVE.

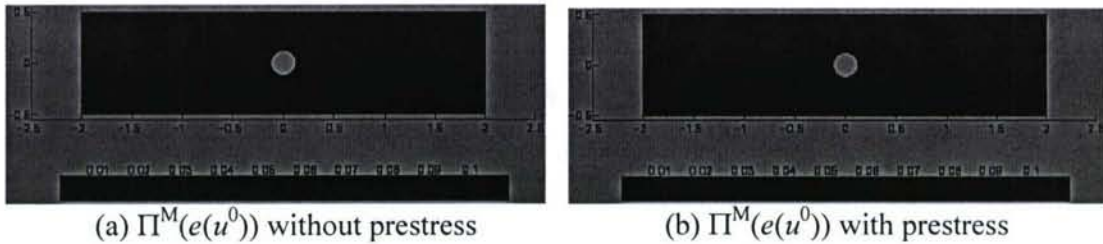


FIGURE 13: The bound for the second strain invariant $\Pi^M(e(u^0))$ in the $+45^\circ$ ply

Failure analysis of a symmetric laminate with an open hole. We compared the normalized bounds of the matrix phase strain invariants with the normalized macro-level stress values and/or their combinations. Experimental strength data were used to back-calculate critical strain invariant values for the matrix phase of the composite. These critical values were used to normalize the strain invariant bounds. Hashin criteria and maximum stress criteria were applied to the ply level (homogenized) stresses. The over-stressed (over-strained) zone is the volume of the composite in which the value of the failure criteria meets or exceeds any of the critical strength parameters (indicated by yellow in Figures 15 – 19).

The computer model for this experiment was identical in dimension to the model of the previous two experiments. The loading, however, was reduced. Since complete

loss of load carrying capacity typically occurs between 0.6% strain and 0.7% strain, we computed over-stressed zones at 0.3% and 0.6% uniaxial tension (applied via displacement on the surface $x = 2$). All other boundary conditions were the same as in the prior experiments.

Figures 14, 15, and 16 display the overstressed zones for the phase strain invariant, Hashin failure criteria, and maximum stress failure criteria, respectively at 0.3% tension strain loading. At such a small loading, the 0° ply has very small overstressed zones just at the hole surface. The 45° ply shows moderately small over-stressed zones protruding from the hole surface out toward the ply edge. The -45° ply (not shown) was similar to the 45° ply, and the 90° ply (also not shown) was almost completely overstressed at just 0.3% strain. The three failure theories agree quite well on the location and size of the over-stressed zones. Moreover, the theories appear to agree on the failure mode. The dashed-line boundary around the macroscopic failure criteria overstrained zone (Figure 14(a)) indicates shear failure. The solid-line boundary around the Hashin overstressed zone (Figure 13(a)) indicates failure via a quadratic combination of transverse tension and in-plane shear forces. The boundary around the maximum stress over-stressed zone (Figure 14(a)) indicates failure by the in-plane shear force. Thus the results suggest that the three theories agree that the shear forces will initiate failure at the hole edge in the 0° ply.

Figures 17, 18, and 19 visualize the over-stressed zones for the micro level strain bounds, Hashin failure criteria, and max stress failure criteria, respectively at 0.6% tension strain loading. The 90° and $\pm 45^\circ$ plies all have large over-stressed zones (only $+45^\circ$ ply is shown). The small overstressed zones very near the hole edge in the 0° ply are the shear overstressed zones seen at 0.3% strain. These shear stresses near the hole edge produce the characteristic cracks running parallel to the fibers in the 0° ply. The slightly larger overstressed zones in the 0° ply appear to be transverse tension failure. These overstressed zones are believed to be an effect of the ply stacking sequence. Once again, the micro-level strain invariants based failure criteria appear to be consistent with the predictions of the Hashin failure criteria and the maximum stress failure criteria. In addition to the three different failure criteria being in agreement on the size and location of the overstressed zones, they also once again appear to agree on the failure mode in each case.

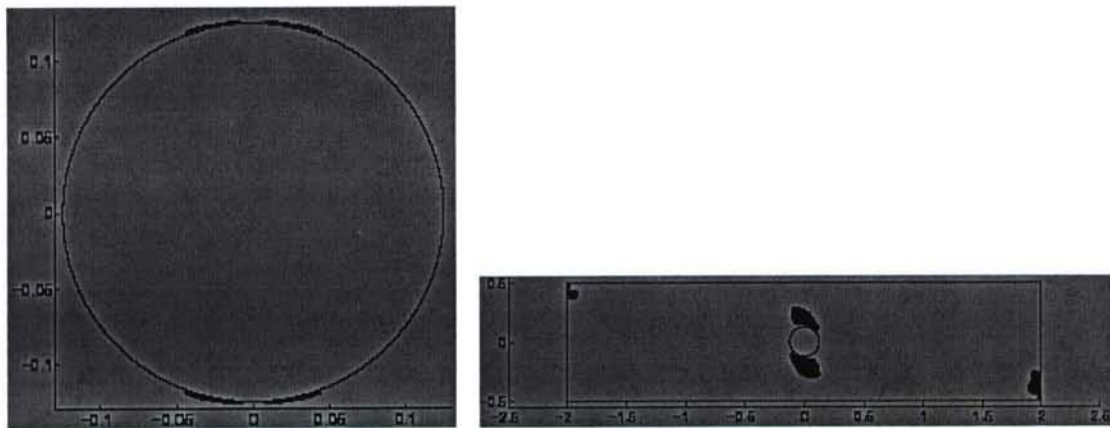




FIGURE 18: Hashin failure criteria overstressed zone at 0.6% strain



FIGURE 19: Maximum stress failure criteria overstressed zone at 0.6% strain

TASK 3. In this task we tried to understand the failure sequence of the composite scarf repair patch and construct a meaningful goal function for strength retention optimization. The main development in this task was to model nonlinear deformation and failure in the adhesive. The deformation of the composite and the patch was modeled with less detail on ply level. We heavily utilized experimental data obtained by Capt. B.M. Cook [8], which included fabrication and testing of the scarf repair as shown on Figure 20.



FIGURE 20. Experimental setup for tensile testing (a) and a plane view of the failed scarf repaired specimen (b).

The key finding in this task was that modeling of the failure of the adhesive in the nonlinear regime is crucial to predicting the strength of the repair. We found that despite

the low stiffness the adhesive transfers enough load in the elastic regime to practically remove the stress concentration due to scarfing and patching thus leading to 95% strength retention prediction. It is the adhesive failure that drastically increases the stress concentration in the parent panel and leads to premature failure. Spline approximation based 3D ply level analysis was used for failure prediction. The plate, adhesive and the repair patch models are shown on Figure 21.

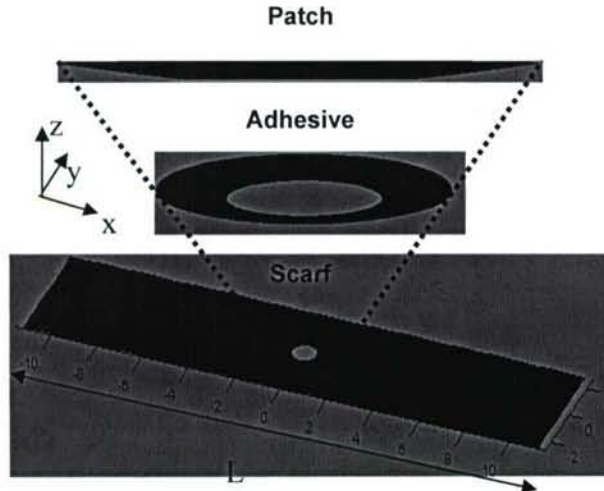


Figure 21. Computational model for the scarfed plate, patch and adhesive.

A nonlinear elastic model was utilized to model the adhesive. At the same time the fiber failure in the scarfed panel was predicted by using the critical failure volume (CFV) method recently proposed in [9-10]. The average applied load for fiber failure was predicted at each load level characterized by a state of delamination in the adhesive/scarfed panel interface. Initially, the stress distribution in the repaired panel is uniform and the fiber failure stress predicted is identical to that of virgin laminate. The increase of the applied load leads to initiation and growth of the delamination between the repair patch and the plate. The stress distribution in the patch becomes nonuniform with the stress concentration typical of open hole composites. At some applied load the average predicted fiber failure load and the applied load become equal. This load value is considered the failure load for the repaired panel.

The unidirectional properties of the IM6/3501-6 material were as follows: $E_{11}=175.27\text{Gpa}$, $E_{22}=E_{33}=9.79\text{Gpa}$, $\nu_{12}=\nu_{13}=0.33$, $\nu_{23}=0.49$, $G_{12}=G_{13}=5.51\text{Gpa}$ and $G_{23}=2.96\text{Gpa}$, with the coefficient of thermal expansion of $\alpha_{11}=4.10^{-6}\text{C}^0$ and $\alpha_{22}=32.10^{-6}\text{C}^0$. The Weibull parameters for the strength in the fiber direction were equal to $X_t=2.06\text{Gpa}$, $V_0=1638.7\text{mm}^3$ and $\alpha=40$. The value of the Weibull modulus was taken from Wisnom et al. [11]. The $l_{min}=0.266\text{mm}$ was calculated according to reference [9-10]. The initial elastic properties of the adhesive were $E=3.1\text{Gpa}$, $\nu=0.38$ and the thermal expansion coefficient was $\alpha=0.7 \cdot 10^{-6}\text{C}^0$. The ply and adhesive thickness were $h=0.13\text{mm}$. The nonlinear shear deformation curve $\tau(\gamma)$ for the FM-300M adhesive was provided by

Structural Integrity Branch of the Air Force Research Laboratory's Materials and Manufacturing Directorate [12] and is shown in Figure 21. Three-dimensional nonlinear deformation of the adhesive was described by assuming nonlinear elasticity with constant Poisson ratio and shear modulus equal to $G = \Gamma(2/\sqrt{3} \varepsilon_{vm})$, where ε_{vm} – is Von-Mises strain, where $G(\gamma) = d\tau(\gamma)/d\gamma$. The temperature change $\Delta T = -155^{\circ}\text{C}$.

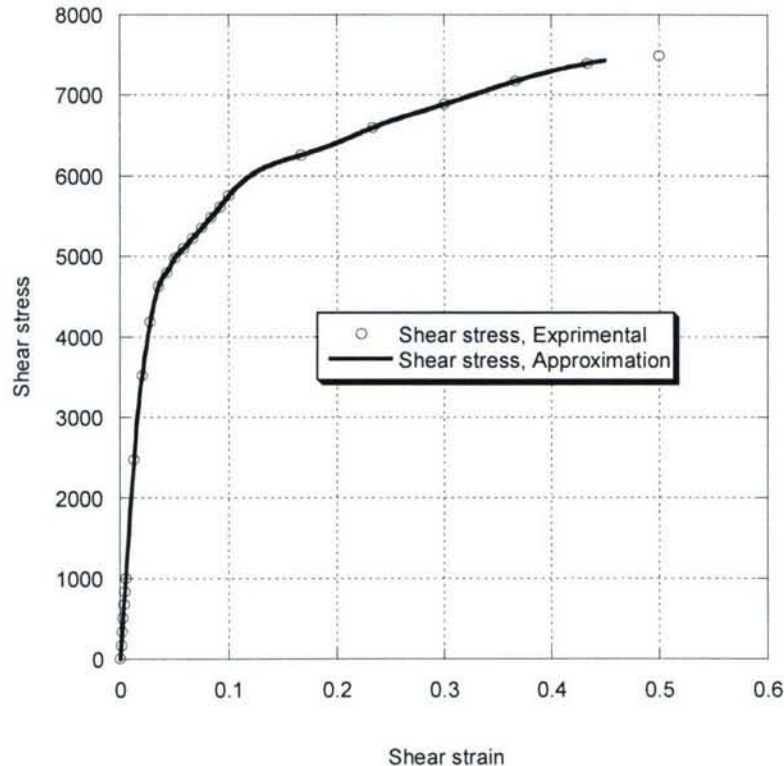


Figure 21. Nonlinear shear deformation curve of the for the FM-300M adhesive.

At low loads prior to the adhesive failure the stress field in the scarfed panel is quite uniform, as shown on the Figure 22. No stress concentration typical of an open hole is present. The average fiber failure load is predicted equal to that of virgin panels.



Figure 22. Normal σ_{xx} stress distribution (a) in the adhesive and (b) the scarfed plate prior to any delamination on the adhesive/panel interface

In the case of scarfed open hole panels a severe stress concentration typical of an open hole exists, Figure 23.a. The strength of such panels is about 1/3 of the virgin panels and is predicted accurately by using the CFV method [9-10]. Thus the strength of the repair is determined by the adhesive failure and/or its nonlinear behavior. The stress distribution in the parent panel corresponding to partially failed adhesive is shown on Figure 23b. This stress concentration is less severe than in the case of open scarfed hole and the predicted strength values of the repaired panels are at the level of 2/3 of the initial virgin panel strength.



Figure 23. Normal σ_{xx} stress distribution in the scarfed and repaired panels. (a) Open scarfed hole and (b) partially delaminated adhesive at 90% of the scarf failure load.

Experimental data and predicted strength values for small and large size unnotched tensile coupons, as well as strength of scarfed open hole and scarfed repaired panels are shown on Figure 24. Significant reduction in experimentally measured strength of large virgin panels as compared to small coupons is attributed to grip failure of most large virgin specimens. Only 5% strength reduction due to volume increase is predicted theoretically. All unrepaired and repaired scarfed laminates exhibited brittle failure through the cavity, thus rendering the test data valid for comparison with theoretical predictions. The predicted strength values for both cases are close to those measured

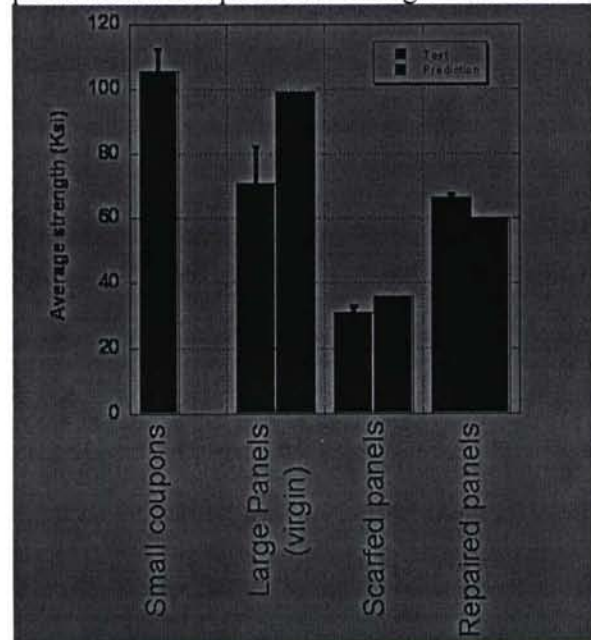


Figure 24. Experimental and numerical results

experimentally.

TASK 4. Development of an automated multiscale mechanism within the B-spline Approximation Method (BSAM) computer program was accomplished ahead of schedule and utilized to produce all results demonstrated in this report.

TASK 5.

In the course of the project, we have understood that our original vision of repair optimization based on elastic properties of adhesive was too simplistic. Indeed as seen from the previous task the repair strength is a direct function of the adhesive failure, which determines the load transfer between the repair patch and the parent laminate. An optimization algorithm which would be based on a repair strength as a goal function will be highly impractical, requiring nonlinear analysis at every optimization iteration and preventing the use of gradient methods [13] for optimization. These complications delayed our progress and required to propose alternative optimization ideas. The one we have selected for implementation is to minimize an elastic L_p norm of a stress invariant failure criteria in the adhesive. Such an approach is targeted to the delay of failure initiation in the adhesive. Although not completed, we have obtained encouraging results. Recall Figure 24, where the predicted strength of the repaired composite was at 60Ksi. This result was obtained for a traditional ply by ply replacement composition of the repair patch. After we switched two ply orientations, namely 0° and 90° inside this patch, we delayed the onset of adhesive failure to 65Ksi. We expect to further delay the adhesive failure by application of the optimization algorithm. These developments are being closely followed by the Structural Integrity Branch of the Air Force Research Laboratory's Materials and Manufacturing Directorate, which is presently conducting an experimental program to verify our findings.

CONCLUSIONS

1) We integrated the rigorous microlevel (fiber, matrix) stress bound estimates by using simply coupled scale analysis, with the spline approximation stress analysis tools - BSAM. A robust multiscale analysis framework was developed and applied within and beyond the scope of the present grant.

2) A key development was the extension of the stress bound estimates in heterogeneous materials with periodic microstructure to include regions of nonperiodic microstructure. Such regions included ply interfaces in fiber reinforced composite materials, which are present in all laminated composite structures. The improved accuracy of the multiscale analysis was verified by comparison with three-dimensional analysis of model cross ply composite laminate, where fibers were modeled explicitly.

3) The developed capabilities were applied to composite scarf repair optimization. Our analysis addressed, for the first time, the composition of the repair patch in addition to more conventional geometric parameters, such as scarf angle and repair depth. We found that altering the conventional ply by ply replacement schema of the repair patch does not lead to premature failure, but delays the failure of the adhesive and increases the

strength of the repaired composite. This work is coordinated with Structural Integrity Branch of the Air Force Research Laboratory's Materials and Manufacturing Directorate, which is presently executing an experimental program to verify our findings.

4) We have transitioned the periodic RVE based micromechanical failure criterion evaluation algorithm to Sikorsky Aircraft, where it was applied to failure analysis of a helicopter flex beam. We are also applying our methodology to investigate applicability of various micromechanical failure criteria to failure prediction of composites under complex states of stress.

REFERENCES

1. Lipton, R. (2003). "Assessment of the Local Stress State through Macroscopic Variables," *Philosophical Transactions of the Royal Society of London A*, 361, pp. 921--946.
2. Lipton, R. (2004)., "Stress Constrained G Closure and Relaxation of Structural Design Problems," *Quarterly of Applied Mathematics*, **62**, 295-321
3. Iarve, E. V. (1996). Spline Variational Three-Dimensional Stress Analysis of Laminated Composite Plates with Open Holes. *Int. J. of Solids and Structures* 33(14) (2095-2117).
4. Iarve, E. V. (1997). Three-Dimensional Stress Analysis in Laminated Composite Plates with Fasteners Based on the B-Spline Approximation. *Composites: Part A*, 28A (559-571).
5. Iarve, E. V., & N. J. Pagano., (2001). Singular Full-Field Stresses in Composite Laminates with Open Holes. *Int. J. Solids Structures* 38(1) (1-28).
6. Gosse, J.H. and Christensen, S. (2001) "Strain Invariant Failure Criteria for Polymers in Composite Material" AIAA-2001-1184, p.11.
7. Sandhu, R.S., Sendeckyj G.P., Schoeppner, G.A. and Papas, J.E. (1992) "Initiation and Prevention of Edge Delamination with and without Residual Stresses" Proceedings of 74th meeting of the Structures and Materials Panel AGARD, AGARD-CP-530, Patras, Greece, 27-28 May 1992
8. Cook, B.M, "Experimentation and Analysis of Composite Scarf Joint," M.S. Thesis, Air Force Institute of Technology, March 2005.
9. Iarve, E.V., Kim, R. and Mollenhauer, D. (2007) "Three-Dimensional Stress Analysis and Weibull Statistics Based Strength Prediction in Open Hole Composite Laminates" *Composite Part A*, **38**, 174-185 .
10. Iarve, E.V., Mollenhauer, D., Whitney, T. and Kim, R. (2006) "Strength Prediction in Composites with Stress Concentrations: Classical Weibull and Critical Failure Volume Methods with Micromechanical Considerations", *J. of Material Science*, **41**(20), pp. 6610-6622
11. Wisnom, M. R., B. Khan, B. Green, W. Jiang and S. R. Hallet (2005), "Specimen Size Effects on Tensile Strength and Failure Mechanisms of

Carbon/Epoxy Composites,” *JNC14 Conference*, Compiegne, March 2005.

- 12. Bolan, B. (2007), “Personal communication”
- 13. Lipton, R. and Stuebner, M., (2006) “Inverse Homogenization and Design of Microstructure for Pointwise Stress Control”, *Qrt. J. Mech. and Appl. Math.*, **59**, pp. 131-169.